INTERNATIONAL JOURNAL FOR NUMERICAL METHODS IN ENGINEERING
Int. J. Numer. Meth. Engng 2012; **89**:269–298
Published online 15 July 2011 in Wiley Online Library (wileyonlinelibrary.com). DOI: 10.1002/nme.3238

An improved continued-fraction-based high-order transmitting boundary for time-domain analyses in unbounded domains

Carolin Birk[1,*,†], Suriyon Prempramote[2] and Chongmin Song[2]

[1]*Institut für Statik und Dynamik der Tragwerke, Fakultät Bauingenieurwesen, Technische Universität Dresden, Dresden, Germany*
[2]*School of Civil and Environmental Engineering, University of New South Wales, Sydney, Australia*

SUMMARY

A high-order local transmitting boundary to model the propagation of acoustic or elastic, scalar or vector-valued waves in unbounded domains of arbitrary geometry is proposed. It is based on an improved continued-fraction solution of the dynamic stiffness matrix of an unbounded medium. The coefficient matrices of the continued-fraction expansion are determined recursively from the scaled boundary finite element equation in dynamic stiffness. They are normalised using a matrix-valued scaling factor, which is chosen such that the robustness of the numerical procedure is improved. The resulting continued-fraction solution is suitable for systems with many DOFs. It converges over the whole frequency range with increasing order of expansion and leads to numerically more robust formulations in the frequency domain and time domain for arbitrarily high orders of approximation and large-scale systems. Introducing auxiliary variables, the continued-fraction solution is expressed as a system of linear equations in iω in the frequency domain. In the time domain, this corresponds to an equation of motion with symmetric, banded and frequency-independent coefficient matrices. It can be coupled seamlessly with finite elements. Standard procedures in structural dynamics are directly applicable in the frequency and time domains. Analytical and numerical examples demonstrate the superiority of the proposed method to an existing approach and its suitability for time-domain simulations of large-scale systems. Copyright © 2011 John Wiley & Sons, Ltd.

Received 6 January 2011; Revised 29 March 2011; Accepted 20 April 2011

KEY WORDS: scaled boundary finite element method; dynamic stiffness; improved continued fraction; transmitting boundary; wave propagation in unbounded domains

1. INTRODUCTION

The numerical modelling of wave propagation in unbounded domains is of importance in many fields of engineering, such as electromagnetics, acoustics, meteorology, geophysics and elastodynamics. Here, the major challenge is the accurate description of radiation damping. Over the past 40 years, major research effort has been devoted to the development of suitable numerical methods. This is reflected in a number of review articles [1–6].

Most of the existing methods can be classified as either exact or approximate methods. In general, exact methods are global in space and time. Therefore, they are computationally expensive for long-time simulations and large-scale problems. A popular method for the analysis of dynamic problems in unbounded media is the boundary element method [7, 8]. Here, a fundamental solution is used, which fulfils the radiation condition at infinity explicitly. However, the evaluation of the fundamental solution is very complicated if the material is anisotropic. The thin-layer method [9–13]

*Correspondence to: Carolin Birk, Institut für Statik und Dynamik der Tragwerke, Fakultät Bauingenieurwesen, Technische Universität Dresden, 01062 Dresden, Germany.
†E-mail: Carolin.Birk@tu-dresden.de

has been developed for wave propagation problems in horizontally layered media. It is based on a combination of a finite element discretisation in the direction of layering with an analytical solution in the wavenumber domain and frequency domain in the direction of wave propagation. Exact non-reflecting boundary conditions, so-called Dirichlet-to-Neumann (DtN) maps [14] have been constructed from analytical solutions for unbounded domains. However, such analytical solutions are available for simple geometries and material properties only.

In general, approximate methods are spatially and temporally local, and thus computationally more efficient than exact methods. They are applied at so-called artificial boundaries. In order to obtain results of acceptable accuracy, these artificial boundaries have to be located sufficiently far away from the domain of interest. The viscous boundary [15] is a classical example. The idea of extending the finite element mesh towards infinity has driven the development of infinite element techniques [5, 16]. In the method of perfectly matched layers [17], the bounded domain is surrounded by a layer of finite thickness that absorbs outgoing waves.

An attractive alternative to the earlier mentioned methods is a high-order local transmitting boundary. It is computationally efficient and leads to accurate results as the order of approximation increases. Early high-order transmitting boundaries include the paraxial boundary [18, 19], the Bayliss–Gunzburger–Turkel (BGT) boundary [20] and the multi-direction boundary [21]. In general, these formulations contain higher-order derivatives. The order of these derivatives increases with the order of transmitting boundary. Terms higher than the second order lead to very complex formulations and instability may occur [22].

These problems led to the idea of introducing auxiliary variables to eliminate the higher-order derivatives in high-order transmitting boundaries. Numerous methods have been developed in this context [23–36]. These are summarised in Reference [37]. Most of these formulations have been developed for scalar waves. In many cases, certain restrictions with respect to the geometry of the boundary are imposed. The extension of the previously discussed high-order local transmitting boundaries to elastic waves in anisotropic unbounded domains of arbitrary geometry is still a challenge.

One idea is to calculate the dynamic stiffness matrix of an unbounded domain for discrete frequencies and to subsequently interpolate these discrete values by a rational function in $\mathrm{i}\omega$. The rational stiffness formulation in the frequency domain corresponds to a system of first-order differential equations in the time domain. This approach has been originally proposed by Wolf [38, 39], who approximated scalar dynamic stiffness coefficients by the ratio of two polynomials. Wolf's idea has been generalised to the multidimensional case by Ruge and co-workers in Reference [40]. There, the fully coupled rational approximation procedure and the subsequent transformation into the time domain have been referred to as the mixed-variables technique. A comprehensive description can be found in Reference [41]. Although the mixed-variables technique leads to efficient time-domain formulations for coupled systems, the calculation of the discrete stiffness values by a suitable numerical method, such as the boundary element method or the scaled boundary finite element method (SBFEM), can be computationally expensive.

The SBFEM [42, 43] is a recent promising method for the dynamic analysis of unbounded domains. Only the boundary is discretised as in the boundary element method, but no fundamental solution is required. General anisotropic materials can be analysed without additional efforts. The SBFEM is extended to the analysis of non-homogeneous unbounded domains with the elasticity modulus and mass density varying as power functions of spatial coordinates in References [44, 45]. The original solution procedure of the scaled boundary finite element (SBFE) equation is global in space and time, and thus computationally expensive. To increase the computational efficiency for large-scale problems, novel solution procedures have been developed recently. Song and Bazyar [46] developed a Padé series solution for the dynamic stiffness matrix of an unbounded domain, which is suitable for frequency-domain analyses. The sparsity and the lumping of the coefficient matrices of the SBFE equation are exploited in [47]. In Reference [37], a continued-fraction solution for the dynamic stiffness is determined directly from the SBFE equation. Here, the computation of the dynamic-stiffness matrix or the unit-impulse response matrix at discrete frequencies or time steps is not required. A high-order local transmitting boundary condition is constructed from the continued-fraction solution of the dynamic stiffness. As a result, the unbounded domain is represented by a system of first-order differential equations in the time domain, which can be coupled to a finite element model of the near field straightforwardly.

The method proposed by Bazyar and Song [37] has been applied successfully to two-dimensional (2D) problems. It is used in combination with the technique of reduced set of base functions to reduce the size of the problem. This facilitates the solution of the dynamic stiffness as continued fractions, but the transmitting boundary has to be placed at a distance away from the interface. Numerical studies [48] reveal that the extension to large-scale problems is challenging. The method may fail for systems with a larger number of DOFs and for approximations of higher-order than those considered in Reference [37]. In such cases, the continued-fraction solution does not converge with increasing order of expansion, and stability problems may occur. Ill-conditioning of the resulting system of first-order differential equations in the time domain has been observed.

The objective of this paper is to develop an improved continued-fraction solution of the SBFE equations in dynamic stiffness, which is numerically more robust and thus suitable for the analysis of three-dimensional (3D) problems.

The further outline of this paper is as follows. The SBFEM is summarised in Section 2. In Section 3, an improved, modified continued-fraction solution for the dynamic stiffness matrix is constructed. A scalar problem with an analytical solution is studied to reveal why the original continued-fraction approach [37] fails in certain situations. Based on this additional insight, a means to improve the numerical robustness of the algorithm is identified. In Section 4, a high-order local transmitting boundary is constructed by using the improved continued-fraction solution and introducing auxiliary variables. The resulting formulation is a system of first-order differential equations in the time domain with symmetric, banded and frequency-independent coefficient matrices. It can be coupled seamlessly with finite elements. The resulting coupled system can be analysed directly in the time domain using standard procedures in structural dynamics. The accuracy of the proposed high-order local transmitting boundary is studied in Section 5. Scalar and 3D numerical examples demonstrate the superiority of the proposed method to the existing approach and its suitability for large-scale systems. Concluding remarks are stated in Section 6.

2. SUMMARY OF THE SCALED BOUNDARY FINITE ELEMENT METHOD

The SBFEM is described in detail in the book [42]. In-depth derivations of the SBFEM for elastodynamics can also be found in References [43, 49]. For completeness, the equations necessary for the development of the high-order local transmitting boundary are summarised briefly in this section.

In the SBFEM, a so-called scaling centre O is chosen in a zone from which the total boundary other than the straight surfaces passing through the scaling centre, must be visible (Figure 1(a)). Only the boundary S visible from the scaling centre O is discretised. Figure 1(b) shows a typical line element to be used in 2D problems, and Figure 1(c) shows a typical surface element to be used in 3D problems. The coordinates of the nodes of an element in a 3D Cartesian coordinate system are arranged in the vectors $\{x\}$, $\{y\}$ and $\{z\}$. The geometry of the isoparametric element is interpolated using the shape functions $[N(\eta,\zeta)]$ formulated in the local coordinates η, ζ of an element on the boundary as

$$\hat{x}(\xi,\eta,\zeta)=\xi[N(\eta,\zeta)]\{x\},\quad \hat{y}(\xi,\eta,\zeta)=\xi[N(\eta,\zeta)]\{y\},\quad \hat{z}(\xi,\eta,\zeta)=\xi[N(\eta,\zeta)]\{z\},\tag{1}$$

where ξ, η and ζ are called the *scaled boundary coordinates*.

The nodal unknown functions $\{u(\xi)\}$ are introduced along the radial lines passing through the scaling centre O and a node on the boundary. These unknowns can be displacements, pressures or temperatures, for example. (The dependency on the excitation frequency ω in a frequency-domain analysis or on time t is omitted from the argument for simplicity when it is not explicitly required.) The unknowns at a point (ξ,η,ζ) are interpolated from the nodal functions $\{u(\xi)\}$ as

$$\{u(\xi,\eta,\zeta)\}=[N^u(\eta,\zeta)]\{u(\xi)\}=[N^1(\eta,\zeta)[I],N^2(\eta,\zeta)[I],...]\{u(\xi)\}.\tag{2}$$

In Equation (2), the size of the identity matrix $[I]$ is $n\times n$, where n is the number of DOFs per node.

DOI: 10.1002/nme

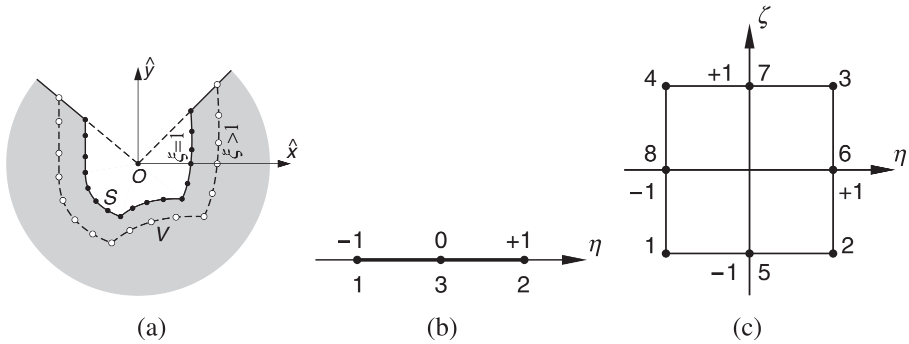

Figure 1. Concept of the scaled boundary finite element method. (a) unbounded domain, (b) three-node line element on boundary of two-dimensional problem, (c) eight-node surface element on boundary of three-dimensional problem.

In a next step, Galerkin's weighted residual technique or the virtual work method is applied in the circumferential directions η, ζ to the governing differential equations. In the frequency domain, the SBFE equation in unknown function $\{u(\xi)\}$ results,

$$
\begin{aligned}
[E^0]\xi^2\{u(\xi)\}_{,\xi\xi} &+ \left((s-1)[E^0] - [E^1] + [E^1]^T\right)\xi\{u(\xi)\}_{,\xi} \\
&+ \left((s-2)[E^1]^T - [E^2]\right)\{u(\xi)\} + \omega^2[M^0]\xi^2\{u(\xi)\} = 0,
\end{aligned}
\tag{3}
$$

where s ($=2$ or 3) denotes the spatial dimension of the domain. $[E^0]$, $[E^1]$, $[E^2]$ and $[M^0]$ are coefficient matrices obtained by assembling the element coefficient matrices as in the finite element method. For 3D acoustic problems, the element coefficient matrices are expressed as

$$[E^0] = \int_{-1}^{+1}\int_{-1}^{+1}[B^1(\eta,\zeta)]^T[B^1(\eta,\zeta)]|J(\eta,\zeta)|\,\mathrm{d}\eta\mathrm{d}\zeta, \tag{4a}$$

$$[E^1] = \int_{-1}^{+1}\int_{-1}^{+1}[B^2(\eta,\zeta)]^T[B^1(\eta,\zeta)]|J(\eta,\zeta)|\,\mathrm{d}\eta\mathrm{d}\zeta, \tag{4b}$$

$$[E^2] = \int_{-1}^{+1}\int_{-1}^{+1}[B^2(\eta,\zeta)]^T[B^2(\eta,\zeta)]|J(\eta,\zeta)|\,\mathrm{d}\eta\mathrm{d}\zeta, \tag{4c}$$

$$[M^0] = \frac{1}{c^2}\int_{-1}^{+1}\int_{-1}^{+1}[N(\eta,\zeta)]^T[N(\eta,\zeta)]|J(\eta,\zeta)|\,\mathrm{d}\eta\mathrm{d}\zeta, \tag{4d}$$

where the symbols $|J(\eta,\zeta)|$ and c represent the determinant of the Jacobian matrix on the boundary and the velocity of wave propagation, respectively. The matrices $[B^1]$ and $[B^2]$, which depend on the geometry of the boundary only, are defined as follows,

$$[B^1] = [b^1][N], \quad [B^2] = [b^2][N_{,\eta}] + [b^3][N_{,\zeta}], \tag{5}$$

with

$$[b^1] = \frac{1}{|J|}\begin{bmatrix} y_{,\eta}z_{,\zeta} - z_{,\eta}y_{,\zeta} \\ z_{,\eta}x_{,\zeta} - x_{,\eta}z_{,\zeta} \\ x_{,\eta}y_{,\zeta} - x_{,\zeta}y_{,\eta} \end{bmatrix}, \; [b^2] = \frac{1}{|J|}\begin{bmatrix} zy_{,\zeta} - yz_{,\zeta} \\ xz_{,\zeta} - zx_{,\zeta} \\ yx_{,\zeta} - xy_{,\zeta} \end{bmatrix}, \; [b^3] = \frac{1}{|J|}\begin{bmatrix} yz_{,\eta} - zy_{,\eta} \\ zx_{,\eta} - xz_{,\eta} \\ xy_{,\eta} - yx_{,\eta} \end{bmatrix}. \tag{6}$$

The element coefficient matrices for 3D elastodynamics are given in Reference [37], for example. The coefficient matrices $[E^0]$ and $[M^0]$ are positive definite. $[E^2]$ is symmetric.

In an elastodynamic problem, the internal nodal forces $\{q(\xi)\}$ on a surface with a constant ξ are obtained by integrating the surface traction over elements. This yields

$$\{q(\xi)\} = \xi^{s-2}\left([E^0]\xi\{u(\xi)\}_{,\xi} + [E^1]^T\{u(\xi)\}\right). \tag{7}$$

DOI: 10.1002/nme

The internal nodal forces are related to the nodal forces $\{R\}$ on the boundary by $\{R\} = -\{q(\xi = 1)\}$ for an unbounded domain. The dynamic stiffness matrix of an unbounded domain $[S^{\infty}(\omega)]$ is defined by

$$\{R(\omega)\} = [S^{\infty}(\omega)]\{u(\omega)\}. \tag{8}$$

In Equation (8), the notations $\{R(\omega)\} = \{R(\xi = 1, \omega)\}$ and $\{u(\omega)\} = \{u(\xi = 1, \omega)\}$ are introduced to denote the force and displacement amplitudes at the boundary. Using Equations (7) and (8), the relationship between the nodal displacements and the radial derivatives of the displacements on the boundary is expressed as

$$[E^0]\{u(\xi, \omega)\}_{,\xi}\big|_{\xi=1} = -\left([S^{\infty}(\omega)] + [E^1]^T\right)\{u(\xi, \omega)\}. \tag{9}$$

Using Equations (7) and (8), the SBFE equation (3) in the unknown function $\{u(\xi)\}$ can be transformed into the so-called SBFE equation in dynamic stiffness (10) (see [42, 43]).

$$\begin{aligned}\left([S^{\infty}(\omega)] + [E^1]\right)[E^0]^{-1}\left([S^{\infty}(\omega)] + [E^1]^T\right) - (s-2)[S^{\infty}(\omega)] - \omega[S^{\infty}(\omega)]_{,\omega}\\ - [E^2] + \omega^2[M^0] = 0.\end{aligned} \tag{10}$$

In an acoustic problem, the unknown quantity in Equation (10) is the impedance matrix of an unbounded domain, which relates the amplitude of the nodal flux $\{R(\omega)\}$ to the amplitudes of the nodal pressure $\{u(\omega)\}$ at the boundary $\xi = 1$.

Equation (10) is a system of non-linear differential equations in the independent variable ω. For $\omega \to \infty$, it can be solved using an asymptotic power expansion [42, 50]. In the rigorous SBFEM, the dynamic stiffness matrix at intermediate and low frequency is obtained by numerical integration of Equation (10). This computationally expensive task is avoided by constructing a continued-fraction solution of the SBFE equation in dynamic stiffness. This is described in detail in the following section.

3. IMPROVED CONTINUED-FRACTION SOLUTION OF DYNAMIC STIFFNESS MATRIX

In this section, a continued-fraction solution for the dynamic stiffness matrix is determined from the SBFE equation in dynamic stiffness. A similar approach has been originally derived by Bazyar and Song [37]. The method proposed in Reference [37], however, has only been used for the analysis of small problems. Only 2D situations have been addressed in Reference [37], which, in combination with the technique of reduced set of base functions, could be reduced to at most 10 DOFs. Parameter studies [48] show that its application to large-scale problems is problematic. For systems with many DOFs and high-orders of expansion, the numerical steps involved in the original continued-fraction approach may become ill-conditioned. As a result, the continued-fraction expansion is erroneous and does not converge. Moreover, ill-conditioning of the resulting equations of motion and instabilities have been observed.

In Section 3.1, a modified continued-fraction expansion of the dynamic stiffness is derived. The robustness of the continued-fraction solution is improved by introducing an additional unknown in the derivation, as will become evident in the following. In Section 3.2, a scalar problem is analysed to identify the reason for the failure of the original continued-fraction approach. Based on the insight gained by studying this model problem, a method for choosing the additional unknown in the multi-dimensional case is proposed in Section 3.3.

3.1. General derivation

The derivation is started by assuming the solution (11)

$$[S^{\infty}(\omega)] = \mathrm{i}\omega\,[C_{\infty}] + [K_{\infty}] - [R^{(1)}(\omega)]. \tag{11}$$

DOI: 10.1002/nme

The first two terms are the constant dashpot and spring matrix, respectively. The term $\left[R^{(1)}(\omega)\right]$ denotes the yet unknown residual of the two-term expansion at high frequency. Substitution of Equation (11) in Equation (10) leads to

$$\begin{aligned}&\left(\mathrm{i}\omega[C_\infty]+[K_\infty]-[R^{(1)}(\omega)]+[E^1]\right)[E^0]^{-1}\left(\mathrm{i}\omega[C_\infty]+[K_\infty]-[R^{(1)}(\omega)]+[E^1]^T\right)\\&\quad-(s-2)\left(\mathrm{i}\omega[C_\infty]+[K_\infty]-[R^{(1)}(\omega)]\right)-\mathrm{i}\omega[C_\infty]+\omega[R^{(1)}]_{,\omega}-[E^2]+\omega^2[M^0]=0.\end{aligned} \quad (12)$$

The terms in Equation (12) can be sorted in descending order of powers of $(\mathrm{i}\omega)$. Equation (12) is satisfied when the two terms corresponding to $(\mathrm{i}\omega)^2$ and $(\mathrm{i}\omega)$ and the remaining lower-order term are equal to zero. Setting the terms corresponding to $(\mathrm{i}\omega)^2$ and $(\mathrm{i}\omega)^1$ equal to zero yields,

$$(\mathrm{i}\omega)^2: \quad 0=[C_\infty][E^0]^{-1}[C_\infty]-[M^0], \quad (13)$$

$$(\mathrm{i}\omega)^1: \quad 0=[C_\infty][E^0]^{-1}\left([K_\infty]+[E^1]^T\right)+\left([K_\infty]+[E^1]\right)[E^0]^{-1}[C_\infty]-(s-1)[C_\infty]. \quad (14)$$

The eigenvalue problem (15) is employed in the solution process.

$$[M^0][\Phi]=[E^0][\Phi]\lceil\Lambda^2\rfloor, \quad \lceil\Lambda^2\rfloor=\mathrm{diag}\left\{\ \lambda_1^2 \quad \lambda_2^2 \quad \cdots \quad \lambda_N^2\ \right\}. \quad (15)$$

The numerical effort required to solve the eigenvalue problem (15) can be reduced by lumping the coefficient matrices $[E^0]$ and $[M^0]$ as proposed in Reference [47]. The eigenvalues $\lceil\Lambda^2\rfloor$ are positive, because both $[M^0]$ and $[E^0]$ are positive definite. Normalising the eigenvectors $[\Phi]$ with respect to the matrix $[E^0]$,

$$[\Phi]^T[E^0][\Phi]=[I], \quad (16)$$

yields

$$[\Phi]^T[M^0][\Phi]=\lceil\Lambda^2\rfloor, \quad (17)$$

$$\left[E^0\right]^{-1}=[\Phi][\Phi]^T. \quad (18)$$

Using Equation (18), pre-multiplying and post-multiplying Equation (13) by $[\Phi]^T$ and $[\Phi]$, respectively, and introducing

$$[c_\infty]=[\Phi]^T[C_\infty][\Phi], \quad [k_\infty]=[\Phi]^T[K_\infty][\Phi], \quad [e^1]=[\Phi]^T[E^1][\Phi], \quad (19)$$

yields

$$[c_\infty]=\lceil\Lambda\rfloor. \quad (20)$$

The matrix $[k_\infty]$ results from:

$$(i\omega)^1: \qquad \lceil\Lambda\rfloor[k_\infty]+[k_\infty]\lceil\Lambda\rfloor=-\lceil\Lambda\rfloor[e^1]^T-[e^1]\lceil\Lambda\rfloor+(s-1)\lceil\Lambda\rfloor. \quad (21)$$

Equation (21) can be solved directly by back substitution as the coefficient matrix at the left-hand side is diagonal. The remaining part of Equation (12) is an equation for $[R^{(1)}(\omega)]$,

$$\begin{aligned}&-\mathrm{i}\omega[C_\infty][E^0]^{-1}[R^{(1)}]+\left([K_\infty]+[E^1]\right)[E^0]^{-1}\left([K_\infty]+[E^1]^T\right)-\mathrm{i}\omega[R^{(1)}][E^0]^{-1}[C_\infty]\\&-\left([K_\infty]+[E^1]\right)[E^0]^{-1}[R^{(1)}]-[R^{(1)}][E^0]^{-1}\left([K_\infty]+[E^1]^T\right)\\&+[R^{(1)}][E^0]^{-1}[R^{(1)}]-(s-2)[K_\infty]+(s-2)[R^{(1)}]+\omega[R^{(1)}]_{,\omega}-[E^2]=0.\end{aligned} \quad (22)$$

The unknown residual $[R^{(1)}(\omega)]$ is expressed as

$$[R^{(i)}(\omega)]=[X^{(i)}][Y^{(i)}(\omega)]^{-1}[X^{(i)}]^T, \quad (23)$$

with $i=1$ and

$$[Y^{(i)}(\omega)]=[Y_0^{(i)}]+\mathrm{i}\omega[Y_1^{(i)}]-[R^{(i+1)}(\omega)]. \quad (24)$$

In Equation (24), the terms $[Y_0^{(i)}]$ and $[Y_1^{(i)}]$ are constants corresponding to the constant and linear term of the ith continued fraction, and $[R^{(i+1)}]$ is the residual of the order i expansion. $[X^{(i)}]$ is a yet undetermined factor. Note that Equations (23) and (24) are identical to the decomposition used in Reference [37] if the factor $[X^{(i)}]$ is chosen as $[X^{(i)}]=[I]$. In this paper, it is selected, such that the robustness of the numerical algorithm is improved.

The derivative $[R^{(i)}]_{,\omega}$ is determined as

$$\begin{aligned}[R^{(i)}(\omega)]_{,\omega} &= [X^{(i)}]([Y^{(i)}(\omega)]^{-1})_{,\omega}[X^{(i)}]^T\\ &= -[X^{(i)}][Y^{(i)}(\omega)]^{-1}[Y^{(i)}(\omega)]_{,\omega}[Y^{(i)}(\omega)]^{-1}[X^{(i)}]^T,\end{aligned} \tag{25}$$

where the derivative $([Y^{(i)}(\omega)]^{-1})_{,\omega}$ can be found in Reference [37]. Using Equations (23) and (25), Equation (22) is reformulated as,

$$\begin{aligned}&-\left\{\mathrm{i}\omega[C_\infty]+[K_\infty]+[E^1]\right\}[E^0]^{-1}[X^{(1)}][Y^{(1)}(\omega)]^{-1}[X^{(1)}]^T\\ &-[X^{(1)}][Y^{(1)}(\omega)]^{-1}[X^{(1)}]^T[E^0]^{-1}\left\{\mathrm{i}\omega[C_\infty]+[K_\infty]+[E^1]^T\right\}\\ &+[X^{(1)}][Y^{(1)}(\omega)]^{-1}[X^{(1)}]^T[E^0]^{-1}[X^{(1)}][Y^{(1)}(\omega)]^{-1}[X^{(1)}]^T\\ &+\left\{[K_\infty]+[E^1]\right\}[E^0]^{-1}\left\{[K_\infty]+[E^1]^T\right\}-(s-2)[K_\infty]+(s-2)[X^{(1)}][Y^{(1)}(\omega)]^{-1}[X^{(1)}]^T\\ &-\omega[X^{(1)}][Y^{(1)}(\omega)]^{-1}[Y^{(1)}]_{,\omega}[Y^{(1)}(\omega)]^{-1}[X^{(1)}]^T-[E^2]=0.\end{aligned} \tag{26}$$

An equation for $[Y^{(1)}(\omega)]$ is obtained by pre-multiplying and post-multiplying Equation (26) by $[Y^{(1)}(\omega)][X^{(1)}]^{-1}$ and $[X^{(1)}]^{-T}[Y^{(1)}(\omega)]$, respectively,

$$\begin{aligned}&+[X^{(1)}]^T[E^0]^{-1}[X^{(1)}]-[Y^{(1)}(\omega)][X^{(1)}]^{-1}\left\{\mathrm{i}\omega[C_\infty]+[K_\infty]+[E^1]\right\}[E^0]^{-1}[X^{(1)}]\\ &-[X^{(1)}]^T[E^0]^{-1}\left\{\mathrm{i}\omega[C_\infty]+[K_\infty]+[E^1]^T\right\}[X^{(1)}]^{-T}[Y^{(1)}(\omega)]\\ &+[Y^{(1)}(\omega)][X^{(1)}]^{-1}\left\{\left([K_\infty]+[E^1]\right)[E^0]^{-1}\left([K_\infty]+[E^1]^T\right)-[E^2]-(s-2)[K_\infty]\right\}[X^{(1)}]^{-T}[Y^{(1)}(\omega)]\\ &+(s-2)[Y^{(1)}(\omega)]-\omega[Y^{(1)}(\omega)]_{,\omega}=0.\end{aligned} \tag{27}$$

Here and in the following, the superscript $-T$ denotes the transpose of the inverse of a matrix. Using Equations (19) and (20), Equation (27) is written as the case $i=1$ of the following equation:

$$\begin{aligned}&[a^{(i)}]-[Y^{(i)}]\left(\mathrm{i}\omega[b_1^{(i)}]^T+[b_0^{(i)}]^T\right)-\left(\mathrm{i}\omega[b_1^{(i)}]+[b_0^{(i)}]\right)[Y^{(i)}]\\ &\quad+[Y^{(i)}][c^{(i)}][Y^{(i)}]-\omega[Y^{(i)}]_{,\omega}=0,\end{aligned} \tag{28}$$

with

$$[a^{(1)}]=[X^{(1)}]^T[\Phi][\Phi]^T[X^{(1)}], \tag{29a}$$

$$[b_1^{(1)}]=[X^{(1)}]^T[\Phi]\lceil\Lambda\rfloor[\Phi]^{-1}[X^{(1)}]^{-T}, \tag{29b}$$

$$[b_0^{(1)}]=[X^{(1)}]^T[\Phi][\Phi]^T\left([K_\infty]+[E^1]^T\right)[X^{(1)}]^{-T}-0.5(s-2)[I], \tag{29c}$$

$$[c^{(1)}]=[X^{(1)}]^{-1}\left\{\left([K_\infty]+[E^1]\right)[\Phi][\Phi]^T\left([K_\infty]+[E^1]^T\right)-(s-2)[K_\infty]-[E^2]\right\}[X^{(1)}]^{-T}. \tag{29d}$$

Using Equation (24), Equation (28) is again expanded to $(\mathrm{i}\omega)^2$, $(\mathrm{i}\omega)$ and remaining lower-order terms,

$$\begin{aligned}&[a^{(i)}]-\left([Y_0^{(i)}]+\mathrm{i}\omega[Y_1^{(i)}]-[R^{(i+1)}(\omega)]\right)\left(\mathrm{i}\omega[b_1^{(i)}]^T+[b_0^{(i)}]^T\right)\\ &\quad-\left(\mathrm{i}\omega[b_1^{(i)}]+[b_0^{(i)}]\right)\left([Y_0^{(i)}]+\mathrm{i}\omega[Y_1^{(i)}]-[R^{(i+1)}(\omega)]\right)\\ &\quad+\left([Y_0^{(i)}]+\mathrm{i}\omega[Y_1^{(i)}]-[R^{(i+1)}(\omega)]\right)[c^{(i)}]\left([Y_0^{(i)}]+\mathrm{i}\omega[Y_1^{(i)}]-[R^{(i+1)}(\omega)]\right)\\ &\quad-\mathrm{i}\omega[Y_1^{(i)}]+\omega[R^{(i+1)}]_{,\omega}=0.\end{aligned} \tag{30}$$

DOI: 10.1002/nme

As for Equation (12), Equation (30) is satisfied when all the three terms in the power series are equal to zero. Setting the $(\mathrm{i}\omega)^2$ term to zero leads to an equation for $[Y_1^{(i)}]$,

$$-[Y_1^{(i)}][b_1^{(i)}]^T-[b_1^{(i)}][Y_1^{(i)}]+[Y_1^{(i)}][c^{(i)}][Y_1^{(i)}]=0. \tag{31}$$

Pre-multiplying and post-multiplying this equation with $[Y_1^{(i)}]^{-1}$ leads to a Lyapunov equation for $[Y_1^{(i)}]^{-1}$,

$$[b_1^{(i)}]^T[Y_1^{(i)}]^{-1}+[Y_1^{(i)}]^{-1}[b_1^{(i)}]=[c^{(i)}] \tag{32}$$

Equating the terms corresponding to $(\mathrm{i}\omega)^1$ to zero yields

$$\begin{aligned}\left(-[b_1^{(i)}]+[Y_1^{(i)}][c^{(i)}]\right)[Y_0^{(i)}]+[Y_0^{(i)}]\left(-[b_1^{(i)}]^T+[c^{(i)}][Y_1^{(i)}]\right)\\ =[Y_1^{(i)}][b_0^{(i)}]^T+[b_0^{(i)}][Y_1^{(i)}]+[Y_1^{(i)}].\end{aligned} \tag{33}$$

This is a Lyapunov equation for $[Y_0^{(i)}]$. The remaining lower-order term,

$$\begin{aligned}&[a^{(i)}]-[Y_0^{(i)}][b_0^{(i)}]^T-[b_0^{(i)}][Y_0^{(i)}]+[R^{(i+1)}(\omega)]\left(\mathrm{i}\omega[b_1^{(i)}]^T+[b_0^{(i)}]^T\right)+\left(\mathrm{i}\omega[b_1^{(i)}]+[b_0^{(i)}]\right)[R^{(i+1)}(\omega)]\\ &\quad+[Y_0^{(i)}][c^{(i)}][Y_0^{(i)}]+[R^{(i+1)}(\omega)][c^{(i)}][R^{(i+1)}(\omega)]-\left([Y_0^{(i)}]+\mathrm{i}\omega[Y_1^{(i)}]\right)[c^{(i)}][R^{(i+1)}(\omega)]\\ &\quad-[R^{(i+1)}(\omega)][c^{(i)}]\left([Y_0^{(i)}]+\mathrm{i}\omega[Y_1^{(i)}]\right)+\omega[R^{(i+1)}(\omega)]_{,\omega}=0,\end{aligned} \tag{34}$$

is reformulated substituting Equation (23) in Equation (34),

$$\begin{aligned}&[a^{(i)}]-[Y_0^{(i)}][b_0^{(i)}]^T-[b_0^{(i)}][Y_0^{(i)}]+[X^{(i+1)}][Y^{(i+1)}(\omega)]^{-1}[X^{(i+1)}]^T\left(\mathrm{i}\omega[b_1^{(i)}]^T+[b_0^{(i)}]^T\right)\\ &\quad+\left(\mathrm{i}\omega[b_1^{(i)}]+[b_0^{(i)}]\right)[X^{(i+1)}][Y^{(i+1)}(\omega)]^{-1}[X^{(i+1)}]^T+[Y_0^{(i)}][c^{(i)}][Y_0^{(i)}]\\ &\quad+[X^{(i+1)}][Y^{(i+1)}(\omega)]^{-1}[X^{(i+1)}]^T[c^{(i)}][X^{(i+1)}][Y^{(i+1)}(\omega)]^{-1}[X^{(i+1)}]^T\\ &\quad-\left([Y_0^{(i)}]+\mathrm{i}\omega[Y_1^{(i)}]\right)[c^{(i)}][X^{(i+1)}][Y^{(i+1)}(\omega)]^{-1}[X^{(i+1)}]^T\\ &\quad-[X^{(i+1)}][Y^{(i+1)}(\omega)]^{-1}[X^{(i+1)}]^T[c^{(i)}]\left([Y_0^{(i)}]+\mathrm{i}\omega[Y_1^{(i)}]\right)\\ &\quad-\omega[X^{(i+1)}][Y^{(i+1)}(\omega)]^{-1}[Y^{(i+1)}(\omega)]_{,\omega}[Y^{(i+1)}(\omega)]^{-1}[X^{(i+1)}]^T=0.\end{aligned} \tag{35}$$

Pre-multiplying and post-multiplying Equation (35) by $[\,Y^{(i+1)}(\omega)\,][X^{(i+1)}]^{-1}$ and $[X^{(i+1)}]^{-T}\times[Y^{(i+1)}(\omega)]$, respectively, yields:

$$\begin{aligned}&[Y^{(i+1)}(\omega)][X^{(i+1)}]^{-1}[a^{(i)}][X^{(i+1)}]^{-T}[Y^{(i+1)}(\omega)]\\ &\quad-[Y^{(i+1)}(\omega)][X^{(i+1)}]^{-1}\left([Y_0^{(i)}][b_0^{(i)}]^T+[b_0^{(i)}][Y_0^{(i)}]-[Y_0^{(i)}][c^{(i)}][Y_0^{(i)}]\right)[X^{(i+1)}]^{-T}[Y^{(i+1)}(\omega)]\\ &\quad+[X^{(i+1)}]^T\left(\mathrm{i}\omega[b_1^{(i)}]^T+[b_0^{(i)}]^T\right)[X^{(i+1)}]^{-T}[Y^{(i+1)}(\omega)]\\ &\quad+[Y^{(i+1)}(\omega)][X^{(i+1)}]^{-1}\left(\mathrm{i}\omega[b_1^{(i)}]+[b_0^{(i)}]\right)[X^{(i+1)}]+[X^{(i+1)}]^T[c^{(i)}][X^{(i+1)}]\\ &\quad-[Y^{(i+1)}(\omega)][X^{(i+1)}]^{-1}\left([Y_0^{(i)}]+\mathrm{i}\omega[Y_1^{(i)}]\right)[c^{(i)}][X^{(i+1)}]\\ &\quad-[X^{(i+1)}]^T[c^{(i)}]\left([Y_0^{(i)}]+\mathrm{i}\omega[Y_1^{(i)}]\right)[X^{(i+1)}]^{-T}[Y^{(i+1)}(\omega)]-\omega[Y^{(i+1)}(\omega)]_{,\omega}=0.\end{aligned} \tag{36}$$

Equation (36) is the $(i+1)$-case of Equation (28),

$$\begin{aligned}[a^{(i+1)}]-[Y^{(i+1)}]\left(\mathrm{i}\omega[b_1^{(i+1)}]^T+[b_0^{(i+1)}]^T\right)-\left(\mathrm{i}\omega[b_1^{(i+1)}]+[b_0^{(i+1)}]\right)[Y^{(i+1)}]\\ +[Y^{(i+1)}][c^{(i+1)}][Y^{(i+1)}]-\omega[Y^{(i+1)}]_{,\omega}=0,\end{aligned} \tag{37}$$

with

$$[a^{(i+1)}] = [X^{(i+1)}]^T [c^{(i)}][X^{(i+1)}] \tag{38a}$$

$$[b_1^{(i+1)}] = [X^{(i+1)}]^T \left(-[b_1^{(i)}]^T + [c^{(i)}][Y_1^{(i)}] \right) [X^{(i+1)}]^{-T}, \tag{38b}$$

$$[b_0^{(i+1)}] = [X^{(i+1)}]^T \left(-[b_0^{(i)}]^T + [c^{(i)}][Y_0^{(i)}] \right) [X^{(i+1)}]^{-T}, \tag{38c}$$

$$[c^{(i+1)}] = [X^{(i+1)}]^{-1} \left([a^{(i)}] - [b_0^{(i)}][Y_0^{(i)}] - [Y_0^{(i)}][b_0^{(i)}]^T + [Y_0^{(i)}][c^{(i)}][Y_0^{(i)}] \right) [X^{(i+1)}]^{-T}. \tag{38d}$$

Equation (37) can be solved by following the same steps as for solving Equation (28). For given coefficients $[X^{(i)}]$, the coefficient matrices $[a^{(i)}]$, $[b_0^{(i)}]$, $[b_1^{(i)}]$ and $[c^{(i)}]$ are evaluated recursively using Equation (38), starting from those at $i = 1$. An order M continued fraction terminates with the approximation $[R^{(M+1)}(\omega)] = 0$. Unlike for the Padé series solution [46], increasing the order of continued fraction does not require the recalculation of the coefficient matrices determined previously for a lower order.

The coefficients $[X^{(i)}]$ are yet undetermined. Note that the algorithm presented earlier reduces to the method presented in Reference [37] if these coefficients are equal to $[X^{(i)}] = [I]$. In this paper, these coefficients are chosen such that the robustness of the approach is improved. To explain the failure of the original continued-fraction approach in some situations and to motivate the proper choice of $[X^{(i)}]$, a scalar model problem is studied in the following.

3.2. *Model problem*

The analysis of a spherical cavity of radius r_0 which is embedded in full space reveals why the original continued-fraction expansion fails in certain situations. The corresponding differential equation in dynamic stiffness is derived in the following. Its continued-fraction solution is addressed in Section 3.2.2.

3.2.1. Scalar wave equation in spherical coordinates. The propagation of sound in an acoustic medium, for example, is governed by the scalar wave equation in three space dimensions,

$$c^2 \nabla^2 u = \ddot{u}, \qquad u = u(r, \phi, \theta, t), \quad \theta \in [0, \pi],\ \phi \in [0, 2\pi], \tag{39}$$

In Equation (39), the symbols u, c and ∇^2 denote the acoustic pressure, the velocity of wave propagation and the Laplacian operator in spherical coordinates, respectively. Equation (39) can be solved analytically using the technique of separation of variables [51]. The solution can be expressed as a sum of modes,

$$u(r, \phi, \theta, t) = \sum_{l=0}^{\infty} \sum_{m=-l}^{+l} \tilde{u}_l(r, t) Y_l^m(\phi, \theta), \tag{40}$$

where the symbol $Y_l^m(\phi, \theta)$ denotes a spherical harmonic function with

$$Y_l^m(\theta, \phi) = N \mathrm{e}^{\mathrm{i}m\phi} P_l^m(\cos\theta). \tag{41}$$

In Equation (41), N is a normalisation constant and P_l^m is an associated Legendre polynomial. The propagation of each mode $\tilde{u}_l(r, t)$ is a one-dimensional problem described by the following scalar differential equation:

$$r^2 \frac{\partial^2 \tilde{u}}{\partial r^2} + 2r \frac{\partial \tilde{u}}{\partial r} - l(l+1)\tilde{u} = \frac{r^2}{c^2} \ddot{\tilde{u}}. \tag{42}$$

The subscript l is dropped in Equation (42) and in the following, for conciseness. In the frequency domain, Equation (42) is expressed as

$$\frac{\mathrm{d}^2 \tilde{U}}{\mathrm{d}r^2} + \frac{2}{r} \frac{\mathrm{d}\tilde{U}}{\mathrm{d}r} - \frac{l(l+1)}{r^2} \tilde{U} + \frac{\omega^2}{c^2} \tilde{U} = 0. \tag{43}$$

Here, the symbol $\tilde{U} = \tilde{U}(r, \omega)$ denotes the amplitude of the modal pressure $\tilde{u} = \tilde{u}(r, t)$. Equation (43) is the spherical Bessel equation. Its solutions are the spherical Bessel functions of the first and second kind, j_l and y_l, respectively, as well as linear combinations of these two functions. For the unbounded domain considered herein, the physically correct solution is

$$\tilde{U} = C h_l^{(2)}(a), \tag{44}$$

with the dimensionless frequency a,

$$a = \frac{\omega r}{c}, \tag{45}$$

and an integration constant C. The symbol $h_l^{(2)}$ denotes the spherical Hankel function of the second kind and order l. The modal flux amplitude $\tilde{R} = \tilde{R}(\omega, r)$ on a sphere of radius r is expressed as

$$\tilde{R} = -r \frac{\mathrm{d}\tilde{U}}{\mathrm{d}r}. \tag{46}$$

Substituting Equation (44) in Equation (46) results in

$$\tilde{R} = -C r \frac{\mathrm{d}h_l^{(2)}}{\mathrm{d}r}. \tag{47}$$

The modal impedance coefficient $S = S(\omega, r)$, which relates the modal flux amplitude to the modal pressure amplitude on a sphere of radius r, is defined as

$$\tilde{R} = S\tilde{U}. \tag{48}$$

Using Equations (48), (47) and (44), it is expressed as

$$S = -\frac{a}{h_l^{(2)}(a)} \frac{\mathrm{d}h_l^{(2)}(a)}{\mathrm{d}a}. \tag{49}$$

Alternatively, a differential equation in dynamic impedance can be derived, which is subsequently expanded into a series of continued fractions. To this end, the modal flux amplitude $\tilde{R}$ is eliminated from Equations (46) and (48),

$$r \frac{\mathrm{d}\tilde{U}}{\mathrm{d}r} = -S\tilde{U}. \tag{50}$$

Differentiating Equation (50) and multiplying the resulting expression by r result in

$$r^2 \frac{\mathrm{d}^2\tilde{U}}{\mathrm{d}r^2} + r\frac{\mathrm{d}\tilde{U}}{\mathrm{d}r} = -Sr\frac{\mathrm{d}\tilde{U}}{\mathrm{d}r} - r\frac{\mathrm{d}S}{\mathrm{d}r}\tilde{U} = \left(S^2 - r\frac{\mathrm{d}S}{\mathrm{d}r}\right)\tilde{U}. \tag{51}$$

Substituting Equation (51) in Equation (43) and eliminating $r\frac{\mathrm{d}\tilde{U}}{\mathrm{d}r}$ using Equation (50), an equation of the impedance coefficient S is obtained,

$$S^2 - S - r\frac{\mathrm{d}S}{\mathrm{d}r} + \left(\frac{\omega r}{c}\right)^2 - l(l+1) = 0. \tag{52}$$

Using Equation (45) and

$$r\frac{\mathrm{d}S}{\mathrm{d}r} = a\frac{\mathrm{d}S}{\mathrm{d}a} = \omega\frac{\mathrm{d}S}{\mathrm{d}\omega}, \tag{53}$$

the equation of the impedance coefficient is formulated in terms of a as,

$$S^2 - S - a\frac{\mathrm{d}S}{\mathrm{d}a} + a^2 - l(l+1) = 0. \tag{54}$$

In order to facilitate its continued-fraction solution, Equation (54) is expressed as

$$(S-0.5)^2 - a\frac{\mathrm{d}S}{\mathrm{d}a} + a^2 - (l+0.5)^2 = 0. \tag{55}$$

Using the following change of variables,

$$S - 0.5 = \bar{S}, \qquad l + 0.5 = \lambda, \tag{56}$$

Equation (55) can be cast in a form that is identical to the equation of the dynamic stiffness of a circular cavity derived in Reference [52].

$$\bar{S}^2 - a\frac{\mathrm{d}\bar{S}}{\mathrm{d}a} + a^2 - \lambda^2 = 0. \tag{57}$$

3.2.2. Continued-fraction expansion. Equation (57) is in a similar form as Equation (10) — only the constant term in $\bar{S}$ is missing. Its order M continued-fraction solution is expressed as

$$\bar{S}(a) = K_\infty + \mathrm{i}aC_\infty - \cfrac{\left(X^{(1)}\right)^2}{Y_0^{(1)} + \mathrm{i}aY_1^{(1)} - \cfrac{\left(X^{(2)}\right)^2}{Y_0^{(2)} + \mathrm{i}aY_1^{(2)} - \cfrac{\left(X^{(3)}\right)^2}{\cdots - \cfrac{\left(X^{(M)}\right)^2}{Y_0^{(M)} + \mathrm{i}aY_1^{(M)}}}}} \tag{58}$$

The continued-fraction solution (58) is constructed in the following using the derivation presented earlier and setting

$$E^0 = 1, \quad E^1 = 0, \quad E^2 = \lambda^2, \quad M^0 = 1, \quad s = 2, \quad \Phi = 1. \tag{59}$$

The coefficients C_∞ and K_∞ follow from Equations (13) and (14), respectively, as

$$C_\infty = 1, \tag{60}$$

$$K_\infty = 0.5. \tag{61}$$

The coefficients $a^{(1)}$, $b_1^{(1)}$, $b_0^{(1)}$ and $c^{(1)}$ are obtained evaluating Equation (29) as

$$a^{(1)} = (X^{(1)})^2, \tag{62a}$$

$$b_1^{(1)} = X^{(1)}C_\infty(X^{(1)})^{-1} = 1.0, \tag{62b}$$

$$b_0^{(1)} = X^{(1)}K_\infty(X^{(1)})^{-1} = 0.5, \tag{62c}$$

$$c^{(1)} = (X^{(1)})^{-1}\left(K_\infty^2 - \lambda^2\right)(X^{(1)})^{-1} = (X^{(1)})^{-1}\left(0.25 - \lambda^2\right)(X^{(1)})^{-1}. \tag{62d}$$

The coefficients $Y_1^{(i)}$ and $Y_0^{(i)}$ follow from Equations (31) and (33), respectively, as

$$Y_1^{(i)} = 2b_1^{(i)}/c^{(i)}. \tag{63a}$$

$$Y_0^{(i)} = \left(2b_0^{(i)} + 1\right)/c^{(i)}, \tag{63b}$$

The recursive equations for the coefficients $a^{(i+1)}$, $b_1^{(i+1)}$, $b_0^{(i+1)}$ and $c^{(i+1)}$ are obtained from Equation (38). Using Equations (63a) and (63b), they can be expressed as

$$a^{(i+1)} = X^{(i+1)}c^{(i)}X^{(i+1)}, \tag{64a}$$

$$b_1^{(i+1)} = X^{(i+1)}b_1^{(i)}(X^{(i+1)})^{-1} = b_1^{(i)}, \tag{64b}$$

$$b_0^{(i+1)} = X^{(i+1)}\left(b_0^{(i)} + 1\right)(X^{(i+1)})^{-1} = b_0^{(i)} + 1, \tag{64c}$$

$$c^{(i+1)} = (X^{(i+1)})^{-1}\left(a^{(i)} + Y_0^{(i)}\right)(X^{(i+1)})^{-1}. \tag{64d}$$

DOI: 10.1002/nme

A further analysis of the coefficients $c^{(i)}$ reveals why the continued-fraction solution fails in certain situations. Using Equations (62b), (62c) and (64b), (64c), respectively, the coefficients $b_1^{(i)}$ and $b_0^{(i)}$ can be explicitly expressed as

$$b_1^{(i)} = 1.0. \tag{65a}$$

$$b_0^{(i)} = i - 0.5. \tag{65b}$$

Using Equation (65a), the coefficient $Y_1^{(i)}$ can be written as

$$Y_1^{(i)} = 2/c^{(i)}. \tag{66}$$

Substituting Equation (65b) in Equation (63b), the coefficient $Y_0^{(i)}$ is expressed as

$$Y_0^{(i)} = 2i/c^{(i)}. \tag{67}$$

Substituting Equation (67) in Equation (64d) and using Equation (64a) yields

$$c^{(i+1)} = (X^{(i+1)})^{-1}\left(X^{(i)}c^{(i-1)}X^{(i)} + \frac{2i}{c^{(i)}}\right)(X^{(i+1)})^{-1}, \tag{68}$$

with $c^{(0)} = 1.0$. Consider a series of coefficients $c^{(i)}$, starting with $i = 1$:

$$c^{(1)} = \left(X^{(1)}\right)^{-1}(0.5^2 - \lambda^2)\left(X^{(1)}\right)^{-1}, \tag{69a}$$

$$c^{(2)} = \left(X^{(2)}\right)^{-1}\left(X^{(1)}X^{(1)} + \frac{2}{\left(X^{(1)}\right)^{-1}(0.5^2 - \lambda^2)\left(X^{(1)}\right)^{-1}}\right)\left(X^{(2)}\right)^{-1} \tag{69b}$$

$$= \frac{\left(X^{(2)}\right)^{-1}}{c^{(1)}}(1.5^2 - \lambda^2)\left(X^{(2)}\right)^{-1}, \tag{69c}$$

$$c^{(3)} = \left(X^{(3)}\right)^{-1}\left(X^{(2)}c^{(1)}X^{(2)} + \frac{4}{\frac{\left(X^{(2)}\right)^{-1}(1.5^2-\lambda^2)\left(X^{(2)}\right)^{-1}}{c^{(1)}}}\right)\left(X^{(3)}\right)^{-1} \tag{69d}$$

$$= \frac{\left(X^{(3)}\right)^{-1}}{c^{(2)}}(2.5^2 - \lambda^2)\left(X^{(3)}\right)^{-1} \tag{69e}$$

This scheme can be generalised as follows:

$$c^{(i)} = \frac{\left(X^{(i)}\right)^{-1}}{c^{(i-1)}}\left((i-0.5)^2 - \lambda^2\right)\left(X^{(i)}\right)^{-1} \tag{70}$$

Recall that the coefficient $X^{(i)}$ is equal to 1.0 if the original approach [37] is used. According to Equation (56), the sphere is characterised by parameters $\lambda = l + 0.5$ with $l = 0, 1, 2, \ldots$. It can easily be seen that for $X^{(i)} = 1.0$, the coefficient $c^{(i)}$ is zero if $i = l + 1$. This is undesirable because $c^{(i)} = 0$ leads to $Y_0^{(i)} \to \infty$ and $Y_1^{(i)} \to \infty$ and thus to the breakdown of the continued-fraction algorithm. This singularity can be avoided by choosing the yet undetermined coefficient as

$$X^{(i)} = \sqrt{|(i-0.5)^2 - \lambda^2|}. \tag{71}$$

Substituting Equation (71) in Equation (70) yields

$$c^{(i)} = \frac{\pm 1}{c^{(i-1)}}, \tag{72}$$

with $c^{(1)} = \pm 1.0$. Thus, the proposed approach yields coefficients $c^{(i)} = \pm 1.0$ in each step of the recursive procedure. The corresponding coefficients $Y_0^{(i)}$ and $Y_1^{(i)}$ are obtained as

$$Y_0^{(i)} = \pm 2i, \qquad Y_1^{(i)} = \pm 2. \tag{73}$$

The coefficient $X^{(i)}$ is equal to zero if $i = l + 1$. As a result, the continued-fraction expansion (see Equation (58)) is effectively terminated at $M = l + 1$.

3.3. *Choice of* $[X^{(i)}]$*: extension to the multidimensional case*

More general problems, which cannot be solved using the method of separation of variables, can be analysed using the SBFEM. A SBFE model can represent only a finite number of modes. The finer the mesh, the more modes can be modelled with high accuracy. In the multidimensional case, the coefficient $[c^{(i)}]$ approaches a singular matrix if the original continued-fraction procedure of Reference [37] is used. This leads to the numerical problems described at the beginning of Section 3. On the contrary, the method proposed in this paper allows the choice of the coefficient $[X^{(i)}]$ such that a robust solution procedure for multidimensional problems is obtained.

In principle, the coefficient $[X^{(i)}]$ can be chosen arbitrarily. In theory, the value of the continued-fraction expansion for a given frequency ω is independent of the choice of $[X^{(i)}]$. However, it is obvious that the choice $[X^{(i)}] = [I]$ leads to numerical difficulties. The analytical study of the scalar differential equation of the modal stiffness coefficient of a spherical cavity reveals that it is advantageous to determine $X^{(i)}$ such that $\left|c^{(i)}\right| = 1$. This idea is extended to the matrix case in the following equation. In each step of the recursive procedure, the coefficient $[c^{(i)}]$ can be expressed as follows:

$$[c^{(i)}] = [X^{(i)}]^{-1}[\tilde{c}^{(i)}][X^{(i)}]^{-T}, \tag{74}$$

with

$$[\tilde{c}^{(i)}] = \left([K_\infty] + [E^1]\right)[\Phi][\Phi]^T\left([K_\infty] + [E^1]^T\right) - (s-2)[K_\infty] - [E^2] \qquad \text{if} \quad i = 1, \tag{75}$$

$$[\tilde{c}^{(i)}] = [a^{(i-1)}] - [b_0^{(i-1)}][Y_0^{(i-1)}] - [Y_0^{(i-1)}][b_0^{(i-1)}]^T + [Y_0^{(i-1)}][c^{(i-1)}][Y_0^{(i-1)}] \quad \text{if} \quad i > 1. \tag{76}$$

The matrix $[\tilde{c}^{(i)}]$ is symmetric. It can be expressed as the product of a lower triangular matrix $[L^{(i)}]$, a diagonal matrix $[D^{(i)}]$ and an upper triangular matrix $[L^{(i)}]^T$,

$$[\tilde{c}^{(i)}] = [L^{(i)}][D^{(i)}][L^{(i)}]^T, \tag{77}$$

using the so-called $\mathbf{LDL}^T$-decomposition, see [53], Section 5.1, page 82. Here, $[L^{(i)}]$ is normalised such that the entries of the diagonal matrix $[D^{(i)}]$ are ± 1.0. The $\mathbf{LDL}^T$-decomposition of a matrix $[A]$ is a generalisation of the Cholesky decomposition, which is applicable even if the matrix $[A]$ is indefinite. Choosing

$$[X^{(i)}] = [L^{(i)}], \tag{78}$$

yields

$$[c^{(i)}] = [L^{(i)}]^{-1}[L^{(i)}][D^{(i)}][L^{(i)}]^T[L^{(i)}]^{-T} = [D^{(i)}]. \tag{79}$$

Thus, the coefficient $[c^{(i)}]$ is diagonal with entries $c_{kk}^{(i)} = \pm 1.0$. The proposed numerical algorithm for the construction of a robust continued-fraction solution of Equation (10) is summarised subsequently.

Algorithm

(1) Solve eigenvalue problem

$$[M^{(0)}][\Phi] = [E^{(0)}][\Phi]\lceil \Lambda^2 \rfloor. \tag{80}$$

Normalise $[\Phi]^T[E^{(0)}][\Phi] = [I]$.

(2) Calculate $[C_\infty]$ using the eigenvalues $\lceil \Lambda \rfloor$ and eigenvectors $[\Phi]$,

$$[c_\infty] = \lceil \Lambda \rfloor = \operatorname{diag}\left\{ \lambda_1 \quad \lambda_2 \quad \cdots \quad \lambda_N \right\}, \quad [C_\infty] = [\Phi]^{-T}[c_\infty][\Phi]^{-1}. \tag{81}$$

DOI: 10.1002/nme

(3) Solve Lyapunov equation for $[k_\infty]$ by back substitution, with $[e^1] = [\Phi]^T [E^1][\Phi]$,

$$\lceil\Lambda\rfloor[k_\infty] + [k_\infty]\lceil\Lambda\rfloor = -\lceil\Lambda\rfloor[e^1]^T - [e^1]\lceil\Lambda\rfloor + (s-1)\lceil\Lambda\rfloor. \tag{82}$$

(4) Calculate $[K_\infty] = [\Phi]^{-T}[k_\infty][\Phi]^{-1}$.
(5) Initialise:

$$\begin{aligned}
&[\tilde{a}^{(1)}] = [\Phi][\Phi]^T,\\
&[\tilde{b}_1^{(1)}] = [\Phi]\lceil\Lambda\rfloor[\Phi]^{-1},\\
&[\tilde{b}_0^{(1)}] = [\Phi][\Phi]^T\left([K_\infty] + [E^1]^T\right) - 0.5(s-2)[I],\\
&[\tilde{c}^{(1)}] = \left([K_\infty] + [E^1]\right)[\Phi][\Phi]^T\left([K_\infty] + [E^1]^T\right) - (s-2)[K_\infty] - [E^2].
\end{aligned}$$

(6) Decompose:

$$[\tilde{c}^{(1)}] = [L^{(1)}][D^{(1)}][L^{(1)}]^T. \tag{83}$$

(7) Choose:

$$[X^{(1)}] = [L^{(1)}]. \tag{84}$$

(8) Update:

$$\begin{aligned}
&[a^{(1)}] = [X^{(1)}]^T[\tilde{a}^{(1)}][X^{(1)}],\\
&[b_1^{(1)}] = [X^{(1)}]^T[\tilde{b}_1^{(1)}][X^{(1)}]^{-T},\\
&[b_0^{(1)}] = [X^{(1)}]^T[\tilde{b}_0^{(1)}][X^{(1)}]^{-T},\\
&[c^{(1)}] = [D^{(1)}].
\end{aligned}$$

(9) For $i = 1, 2, \cdots, M$:
   (a) Solve Lyapunov equation for $\left[Y_1^{(i)}\right]^{-1}$,

$$[b_1^{(i)}]^T[Y_1^{(i)}]^{-1} + [Y_1^{(i)}]^{-1}[b_1^{(i)}] = [c^{(i)}].$$

   (b) Solve Lyapunov equation for $\left[Y_0^{(i)}\right]$,

$$\begin{aligned}
&\left(-[b_1^{(i)}] + [Y_1^{(i)}][c^{(i)}]\right)[Y_0^{(i)}] + [Y_0^{(i)}]\left(-[b_1^{(i)}]^T + [c^{(i)}][Y_1^{(i)}]\right)\\
&\quad = [Y_1^{(i)}][b_0^{(i)}]^T + [b_0^{(i)}][Y_1^{(i)}] + [Y_1^{(i)}].
\end{aligned}$$

   (c) Compute recursively:

$$\begin{aligned}
&[\tilde{a}^{(i+1)}] = [c^{(i)}],\\
&[\tilde{b}_1^{(i+1)}] = -[b_1^{(i)}]^T + [c^{(i)}][Y_1^{(i)}],\\
&[\tilde{b}_0^{(i+1)}] = -[b_0^{(i)}]^T + [c^{(i)}][Y_0^{(i)}],\\
&[\tilde{c}^{(i+1)}] = [a^{(i)}] - [b_0^{(i)}][Y_0^{(i)}] - [Y_0^{(i)}][b_0^{(i)}]^T + [Y_0^{(i)}][c^{(i)}][Y_0^{(i)}].
\end{aligned}$$

   (d) Decompose:

$$[\tilde{c}^{(i+1)}] = [L^{(i+1)}][D^{(i+1)}][L^{(i+1)}]^T. \tag{85}$$

   (e) Choose:

$$[X^{(i+1)}] = [L^{(i+1)}]. \tag{86}$$

DOI: 10.1002/nme

(f) Update:

$$
\begin{aligned}
[a^{(i+1)}] &= [X^{(i+1)}]^T [\tilde{a}^{(i+1)}][X^{(i+1)}],\\
[b_1^{(i+1)}] &= [X^{(i+1)}]^T [\tilde{b}_1^{(i+1)}][X^{(i+1)}]^{-T},\\
[b_0^{(i+1)}] &= [X^{(i+1)}]^T [\tilde{b}_0^{(i+1)}][X^{(i+1)}]^{-T},\\
[c^{(i+1)}] &= [D^{(i+1)}].
\end{aligned}
$$

Continue.

Note that in Reference [37], the coefficient $[b_1^{(i)}]$ is expressed as an eigenvalue decomposition and used subsequently to transform the Lyapunov equations for $[Y_1^{(i)}]^{-1}$ (Equation (32)) and $[Y_0^{(i)}]$ (Equation (33)) in diagonal form, which can be solved by back substitution. This should be avoided here because in decomposing, for example, $[b_1^{(1)}]$ as

$$[b_1^{(1)}] = [V^{(1)}]\lceil\Lambda\rfloor[V^{(1)}]^{-1} = [X^{(1)}]^T[\Phi]\lceil\Lambda\rfloor[\Phi]^{-1}[X^{(1)}]^{-T},$$

the effect of the additional parameter $[X^{(i)}]$ is cancelled, and the task of solving Equations (32) and (33) is transformed into the ill-conditioned problem of Reference [37].

This algorithm indicates that the computational cost associated with the calculation of the coefficient matrices of the continued-fraction expansion depends on the total number of DOFs N and on the order of expansion M. To start the process, an eigenvalue problem and a Lyapunov equation of order N have to be solved. After that, an $\mathbf{LDL}^T$-decomposition and the solution of two Lyapunov equations of order N is required for each $i = 1$ to M, Thus, the computational effort to calculate the coefficients $[Y_0^{(i)}]$ and $[Y_1^{(i)}]$ is directly proportional to the order of continued-fraction M. Note that increasing M does not require the recalculation of the coefficient matrices determined previously, unlike for the Padé series solution presented in Reference [46].

Once the coefficients of the continued-fraction solution have been calculated, a temporally local time-domain representation of the unbounded medium is immediately available. This is based on the use of auxiliary variables, as is demonstrated in the next section. A comparable method with auxiliary variables has been proposed by Ruge *et al.* [40]. In Reference [40], a rational interpolation of discrete values of the dynamic stiffness matrix is employed, which are obtained by numerically integrating the SBFE equation in dynamic stiffness. For large-scale problems, this is considerably more expensive than the approach proposed in this paper. Moreover, increasing the order of continued-fraction M requires the repeated solution of a corresponding least-squares problem and an associated algebraic splitting process, although the same input data can be used.

4. CONSTRUCTION OF HIGH-ORDER LOCAL TRANSMITTING BOUNDARY

Starting from the continued-fraction solution of the dynamic stiffness matrix $[S^\infty]$, a high-order local transmitting boundary formulation can be constructed as an equation of motion. The resulting coefficient matrices are frequency independent and symmetric. This high-order transmitting boundary modelling the unbounded domain can be coupled seamlessly and straightforwardly with finite elements modelling the near field. It is obtained analogously from Reference [37].

The first term of the continued-fraction solution (11) is substituted in the force-displacement relationship on the boundary ($\xi = 1$),

$$\{R(\omega)\} = [S^\infty(\omega)]\{u(\omega)\} = (\mathrm{i}\omega[C_\infty] + [K_\infty])\{u(\omega)\} - [X^{(1)}]\{u^{(1)}(\omega)\}, \tag{87}$$

where the auxiliary variable $\{u^{(1)}(\omega)\}$ is defined as

$$\{u^{(1)}(\omega)\} = [Y^{(1)}(\omega)]^{-1}[X^{(1)}]^T\{u(\omega)\}, \tag{88}$$

or

$$\{u(\omega)\} = [X^{(1)}]^{-T}[Y^{(1)}(\omega)]\{u^{(1)}(\omega)\}. \tag{89}$$

DOI: 10.1002/nme

Using Equation (24) and pre-multiplying Equation (89) by $[X^{(1)}]^T$, it can be written as

$$[X^{(1)}]^T\{u(\omega)\} = \left([Y_0^{(1)}] + \mathrm{i}\omega[Y_1^{(1)}]\right)\{u^{(1)}(\omega)\} - [X^{(2)}]\{u^{(2)}(\omega)\}, \tag{90}$$

where the auxiliary variable $\{u^{(2)}(\omega)\}$ is defined as

$$\{u^{(1)}(\omega)\} = [X^{(2)}]^{-T}[Y^{(2)}(\omega)]\{u^{(2)}(\omega)\}. \tag{91}$$

Equations (90) and (91) can be generalised as

$$[X^{(i)}]^T\{u^{(i-1)}(\omega)\} = \left([Y_0^{(i)}] + \mathrm{i}\omega[Y_1^{(i)}]\right)\{u^{(i)}(\omega)\} - [X^{(i+1)}]\{u^{(i+1)}(\omega)\}, \tag{92}$$

where the auxiliary variable $\{u^{(i+1)}(\omega)\}$ is defined as

$$\{u^{(i)}(\omega)\} = [X^{(i+1)}]^{-T}[Y^{(i+1)}(\omega)]\{u^{(i+1)}(\omega)\}. \tag{93}$$

In Equation (92), $\{u^{(0)}(\omega)\} = \{u(\omega)\}$ is introduced to denote the displacement on the boundary. An order M continued fraction terminates with the approximation $\{u^{(M+1)}(\omega)\} = 0$. The force-displacement relationship on the boundary in Equation (87) and the relationships among the auxiliary variables in Equation (92) can be combined into a matrix form for an order M continued fraction as

$$([A] + \mathrm{i}\omega[B])\{Z(\omega)\} = \{F(\omega)\} \tag{94}$$

with the frequency-independent coefficient matrices $[A]$, $[B]$, the function $\{Z(\omega)\}$ and the external excitation $\{F(\omega)\}$ defined as

$$[A] = \begin{bmatrix} [K_\infty] & -[X^{(1)}] & 0 & \cdots & 0 & 0 \\ -[X^{(1)}]^T & [Y_0^{(1)}] & -[X^{(2)}] & \cdots & 0 & 0 \\ 0 & -[X^{(2)}]^T & [Y_0^{(2)}] & \cdots & 0 & 0 \\ \vdots & \vdots & \vdots & \ddots & -[X^{(M-1)}] & 0 \\ 0 & 0 & 0 & -[X^{(M-1)}]^T & [Y_0^{(M-1)}] & -[X^{(M)}] \\ 0 & 0 & 0 & 0 & -[X^{(M)}]^T & [Y_0^{(M)}] \end{bmatrix}, \tag{95a}$$

$$[B] = \mathrm{diag}\left([C_\infty], [Y_1^{(1)}], [Y_1^{(2)}], \cdots, [Y_1^{(M-1)}], [Y_1^{(M)}]\right), \tag{95b}$$

$$\{Z(\omega)\} = \left\{ \begin{matrix} \{u(\omega)\} \\ \{u^{(1)}(\omega)\} \\ \{u^{(2)}(\omega)\} \\ \vdots \\ \{u^{(M-1)}(\omega)\} \\ \{u^{(M)}(\omega)\} \end{matrix} \right\}, \quad \{F(\omega)\} = \left\{ \begin{matrix} \{R(\omega)\} \\ 0 \\ 0 \\ \vdots \\ 0 \\ 0 \end{matrix} \right\}. \tag{95c}$$

Equation (94) is a standard equation of motion of a linear system in structural dynamics written in the frequency domain. It is expressed in the time domain as a high-order temporally local transmitting boundary condition

$$[A]\{z(t)\} + [B]\{\dot{z}(t)\} = \{F(t)\} \tag{96}$$

Both the tri-block-diagonal matrix $[A]$ and the block-diagonal matrix $[B]$ are symmetric and banded. The half band width is equal to the number of DOFs on the near field / far field interface. Equations (94) and (96) can be assembled with finite elements straightforwardly when the same shape functions are employed at the common boundary. The resulting equation of motion for the global system

DOI: 10.1002/nme

can be solved by standard time-stepping procedures, such as Newmark's method. Thus, the response to arbitrary transient loads can be computed efficiently. Nonlinearities in the near field can also be included. The numerically expensive task of evaluating convolution integrals is not required. The gain with respect to computational efficiency due to the direct formulation in the time domain is enormous, in particular, for large-scale systems, small time-steps or long simulation times. The system (96) is stable when all the eigenvalues of the general eigenproblem for $[A]$ and $[B]$ have negative real parts, which can be verified before computing the response. Possible spurious modes can be eliminated using the spectral shifting technique proposed in Reference [41].

5. NUMERICAL EXAMPLES

In this section, the accuracy of the proposed improved high-order local transmitting boundary in both frequency and time domains is evaluated by numerical examples. Its superiority with respect to the original continued-fraction approach [37] is demonstrated. A one-dimensional example, for which an analytical solution is available, is analysed in Section 5.1. For this example, a single mode of a spherical cavity embedded in full space, the original approach fails completely. A SBFE model of the same system is addressed in Section 5.2 to demonstrate the capacity of the high-order transmitting boundary for systems with many DOFs, where the original formulation leads to ill-conditioning. In Section 5.3, a 3D elastodynamic problem is analysed in both frequency domain and time domain.

To provide a reference solution for the 3D examples, the rigorous, spatially and temporally global solution procedure is applied. In a frequency-domain analysis, the dynamic stiffness matrix at a high but finite frequency is evaluated by using the first four terms of the asymptotic expansion for high frequency as described in [42]. It provides a starting value to numerically integrate the SBFE equation in dynamic stiffness (Equation (10)) to determine the dynamic stiffness matrix at intermediate and low frequencies. In a time-domain analysis, the SBFE equation in dynamic stiffness is transformed to one in unit-impulse response [42]. After time discretisation, the unit-impulse response matrix at discrete time stations is computed step by step. A transient response is then evaluated from the nodal force-nodal displacement relationship expressed as a convolution integral.

5.1. Single mode of spherical cavity embedded in full space

A single mode l of the spherical cavity described in Section 3.2 is analysed in more detail in the following. The modal impedance coefficients for modes $l = 1, 2, 5$ and 12 are calculated from the proposed improved continued-fraction solution in Equation (58) with the coefficients in Equations (71) and (73). The results are non-dimensionalised using the parameter $\lambda = l + 0.5$. The real and imaginary parts of the non-dimensionalised modal impedance coefficients are compared with the exact solution (Equation (49)) in Figures 2–5.

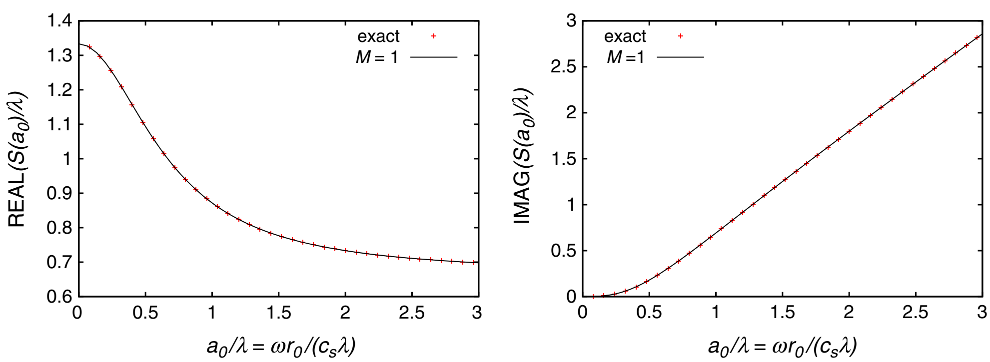

Figure 2. Continued-fraction solution for modal impedance coefficient of spherical cavity ($l = 1$, $\lambda = 1.5$).

DOI: 10.1002/nme

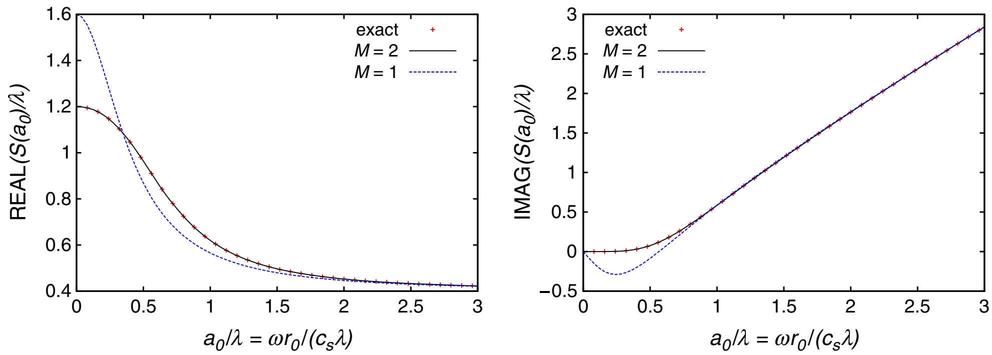

Figure 3. Continued-fraction solution for modal impedance coefficient of spherical cavity ($l = 2$, $\lambda = 2.5$).

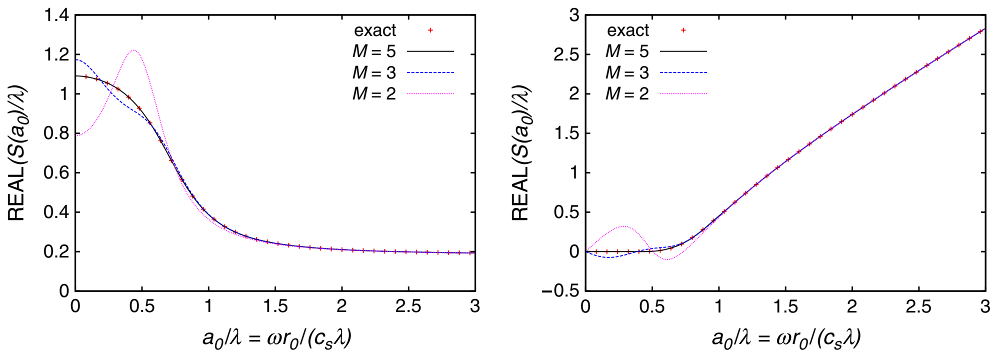

Figure 4. Continued-fraction solution for modal impedance coefficient of spherical cavity ($l = 5$, $\lambda = 5.5$).

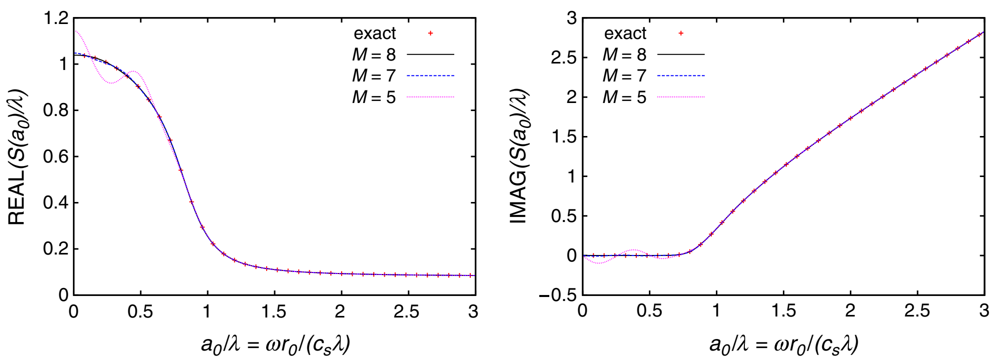

Figure 5. Continued-fraction solution for modal impedance coefficient of spherical cavity ($l = 12$, $\lambda = 12.5$).

As explained earlier, a continued-fraction expansion of degree $M = l$ solves the differential equation (54) in modal impedance coefficient S exactly. This is clearly visible in Figures 2–4. For high mode numbers l, the high-frequency continued-fraction solution converges to the exact solution for lower orders $M < l$ already. This is illustrated in Figure 5. For $l = 12$, the agreement between the exact modal impedance and a continued-fraction solution of order $M = 8$ is very good. This is in accordance with the results of a parametric study on the order of an equivalent Padé series required to achieve a given accuracy presented in Reference [46].

Recall that in the original continued-fraction approach [37], the coefficient $X^{(i)}$ is equal to 1.0, which leads to the failure of the numerical algorithm if the order of continued-fraction expansion M is higher than the mode number l. The exact eigenvalues $l = 0, 1, 2, \ldots$ of a sphere lead to parameters $\lambda = 0.5, 1.5, 2.5 \ldots$, as given in Equation (56). In a numerical model, however, parameters

DOI: 10.1002/nme

λ_{num}, which are close to λ, but slightly perturbed, occur. In this case, the original approach does not break down completely, but it leads to coefficients $Y_0^{(i)}$, $Y_1^{(i)}$, which vary strongly in magnitude in each step of the recursive procedure. For $l = 2$, this is illustrated in Table I, which contains the coefficients $X^{(i)}$, $c^{(i)}$, $Y_0^{(i)}$ and $Y_1^{(i)}$ computed using the original continued-fraction approach [37] and the proposed improved method. The fifth column in Table I shows that, starting with $i = 3$, the coefficients $c^{(i)}$, $Y_0^{(i)}$ and $Y_1^{(i)}$ differ in magnitude by approximately a factor of 10^9, in each step of the recursive procedure. In the matrix case, this causes the numerical problems described in Section 3.

The transient response of the spherical cavity, initially at rest, to an impulse of modal flux $q(t)$ shown in Figure 6 is evaluated. The duration of the impulse is $4r_0/c$. The peak value is Q_0. The dimensionless Fourier transform $Q(a)$ of the impulse $q(t)$ is also shown. It is defined as

$$Q(a) = \int_{-\infty}^{+\infty} q(\bar{t})\mathrm{e}^{-\mathrm{i}a\bar{t}}\,\mathrm{d}\bar{t}. \tag{97}$$

The exact solution for pressure response $u(t)$ is evaluated by performing the inverse Fourier transformation on $U(\omega) = Q(\omega)/S_{ex}(\omega)$, where $S_{ex}(\omega)$ is the exact solution of the modal impedance coefficient in Equation (49). The numerical result is computed by applying the high-order transmitting boundary condition (Equation (96)) directly on the cavity wall. The coefficient matrices $[A]$ and $[B]$ in Equation (96) are formed using the coefficients in Equations (63). $[A]$ is diagonal and $[B]$ is tri-diagonal. A standard time-stepping scheme is used to integrate Equation (96). The time step is chosen as $0.01r_0/c$. The pressure response is non-dimensionalised by Q_0. The results are shown in Figures 7–10 for modes n =1, 2, 5 and 12, together with the exact solution. As explained earlier, the numerical solution is identical to the exact solution if the order of approximation M is equal to the mode number l. For high mode numbers, the results converge to the exact solutions, as the order of the transmitting boundary increases, even for $M < l$. As an example, the agreement between

Table I. Comparison of coefficients $X^{(i)}$, $c^{(i)}$, $Y_0^{(i)}$ and $Y_1^{(i)}$ obtained using the original continued-fraction approach [37] and the proposed improved method ($l = 2$).

	Present method		Original approach [37]	
$l = 2$	$\lambda = 2.5$	$\lambda = 2.50001$	$\lambda = 2.5$	$\lambda = 2.50001$
$c^{(1)}$	−1.0000000000000	−1.0000000000000	−6.0000000000000	−6.0000500001000
$X^{(1)}$	+2.4494897427832	+2.4494999489896	+1.0000000000000	+1.0000000000000
$Y_0^{(1)}$	−2.0000000000000	−2.0000000000000	−0.3333333333333	−0.3333305555731
$Y_1^{(1)}$	−2.0000000000000	−2.0000000000000	−0.3333333333333	−0.3333305555731
$c^{(2)}$	+1.0000000000000	+1.0000000000000	+0.6666666666667	+0.6666694444269
$X^{(2)}$	+2.0000000000000	+2.0000124999859	+1.0000000000000	+1.0000000000000
$Y_0^{(2)}$	+4.0000000000000	+4.0000000000000	+6.0000000000000	+5.9999750002625
$Y_1^{(2)}$	+2.0000000000000	+2.0000000000000	+3.0000000000000	+2.9999875001313
$c^{(3)}$	+1.0000000000000	−1.0000000000000	0.0000000000000	−7.49998375E−005
$X^{(3)}$	+0.0000000000000	+7.071074883E−03	+1.0000000000000	+1.0000000000000
$Y_0^{(3)}$	+6.0000000000000	−6.0000000000000	∞	−80000.1733313043
$Y_1^{(3)}$	+2.0000000000000	−2.0000000000000	∞	−26666.7244437681
$c^{(4)}$	+1.0000000000000	−1.0000000000000		−79999.506661860
$X^{(4)}$	+2.4494897427832	+2.4494795365342		+1.0000000000000
$Y_0^{(4)}$	+8.0000000000000	−8.0000000000000		−1.00000617E−004
$Y_1^{(4)}$	+2.0000000000000	−2.0000000000000		−2.50001542E−005
$c^{(5)}$	+1.0000000000000	−1.0000000000000		−1.75000454E−004
$X^{(5)}$	+3.7416573867739	+3.7416507052236		+1.0000000000000
$Y_0^{(5)}$	+10.000000000000	−10.000000000000		−57142.708839983
$Y_1^{(5)}$	+2.0000000000000	−2.0000000000000		−11428.541767997

DOI: 10.1002/nme

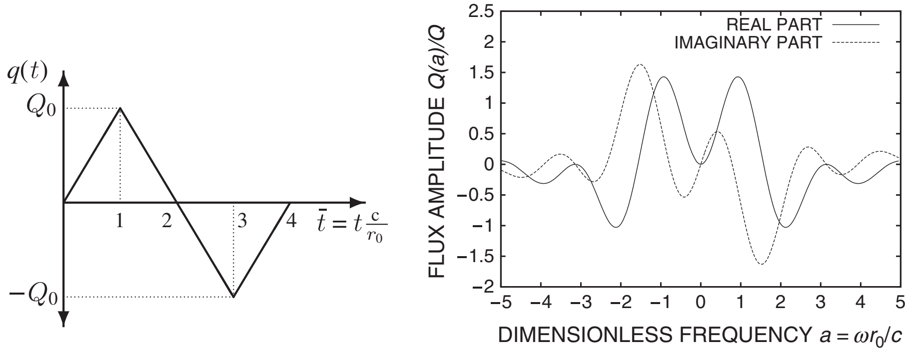

Figure 6. Flux impulse: time history and dimensionless Fourier transform.

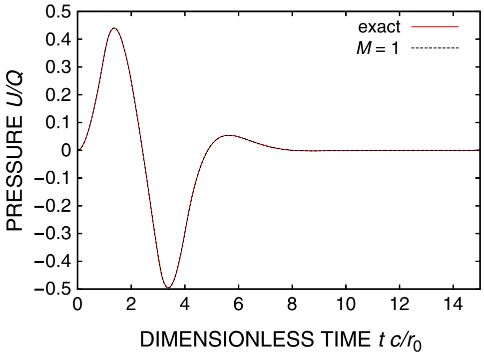

Figure 7. Modal pressure response of a spherical cavity to flux impulse shown in Figure 6; mode $l = 1$.

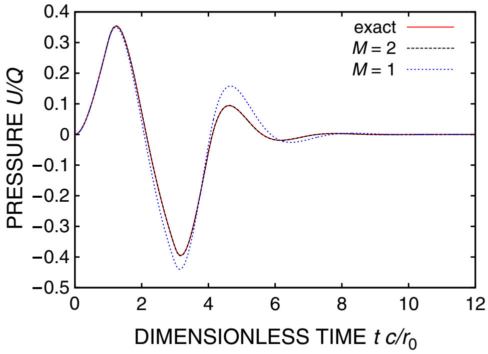

Figure 8. Modal pressure response of a spherical cavity to flux impulse shown in Figure 6; mode $l = 2$.

reference solution for mode number $l = 12$ and approximate solution based on $M = 8$ agree very well, as can be seen in Figure 10.

5.2. *Three-dimensional model of acoustic wave propagation in full space bounded by a sphere*

Acoustic wave propagation in a 3D full space bounded by a sphere of radius r_0 is considered. Assuming symmetric loading, only one octant of the sphere is modelled using the SBFEM. The octant is bounded by three curves which are defined as the intersection of the sphere surface with the xy-plane, yz-plane and xz-plane, respectively. The mesh is constructed by dividing each of these curves into n_s equal sections. The mesh lines are defined as the great circles running from the vertex opposite of one of the intersecting curves to the nodes defined by the sections of the same curve. This is illustrated schematically in Figure 11 for $n_s = 2$. In the example considered herein, the number of sections is chosen as $n_s = 16$, leading to a total of 169 nodes.

DOI: 10.1002/nme

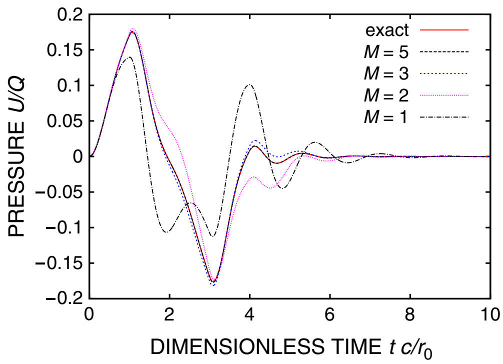

Figure 9. Modal pressure response of a spherical cavity to flux impulse shown in Figure 6; mode $l=5$.

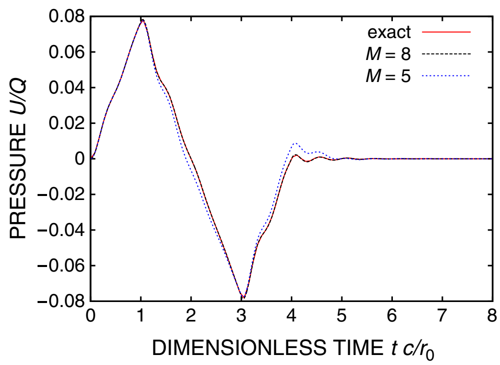

Figure 10. Modal pressure response of a spherical cavity to flux impulse shown in Figure 6; mode $l=12$.

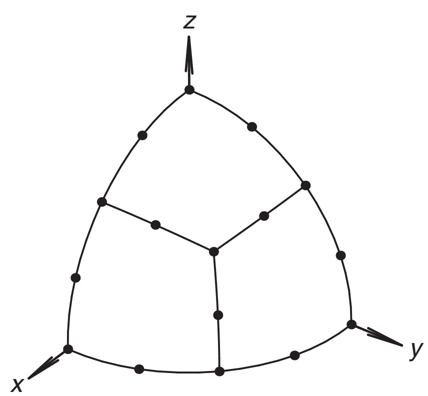

Figure 11. Spherical cavity embedded in full space; example mesh with $n_s = 2$ to illustrate the mesh generation.

This relatively fine SBFE mesh can represent the lower-order modes of the spherical cavity with high accuracy. The approximate modes of the numerical model are calculated by solving the following eigenvalue problem [54],

$$[Z]\{\phi_i\} = \lambda_i\{\phi_i\}, \tag{98}$$

with

$$[Z] = \begin{bmatrix} [E^0]^{-1}[E^1]^T - 0.5(s-2)[I] & -[E^0]^{-1} \\ -[E^2] + [E^1][E^0]^{-1}[E^1]^T & -([E^1][E^0]^{-1} - 0.5(s-2)[I]) \end{bmatrix}. \tag{99}$$

DOI: 10.1002/nme

For the SBFE model with 169 DOFs, the 36 smallest eigenvalues λ are given in Table II. It can be seen that, for the first mode $l=0$, the difference between exact and numerical value is $\varepsilon = 9\cdot 10^{-14}$.

Both the original continued-fraction approach presented in Reference [37] and the proposed method are used to construct continued-fraction solutions of Equation (10). As explained earlier, the original approach may lead to singular coefficients $[c^{(i)}]$, which in turn cause the numerical problems described in Section 3. The singular value decomposition [55] provides a means of measuring how close to a singular matrix $[c^{(i)}]$ is. A singular matrix is characterised by at least one singular value $\sigma=0$. The maximum and minimum singular values of the matrices $[c^{(i)}]$ obtained using the original continued-fraction approach are listed in Table III together with the inverse condition number $1/r_c$ of $[c^{(i)}]$, which is defined as the ratio of the minimum and maximum singular value. A matrix is singular if its inverse condition number $1/r_c$ is zero, and it is ill-conditioned if its inverse condition number is too small, that is, if it approaches the machine's floating point precision (for example 10^{-12} for double precision, see Reference [55]). Table III shows that the inverse condition number obtained for $i=1$ is already relatively small. It decreases further in each step of the recursive procedure. For $i \geqslant 6$, the matrix $[c^{(i)}]$ is ill-conditioned. After $i=12$ steps, it is singular to machine precision.

The problem of ill-conditioning of $[c^{(i)}]$ is completely avoided if the proposed approach is used to calculate the coefficients of the continued-fraction expansion of $[S^{\infty}]$. Here, all singular values of $[c^{(i)}]$ are equal to one, such that $[c^{(i)}]$ is always perfectly well-conditioned.

For further illustration, the elements $Y_0^{(i)}(1,1)$–$Y_0^{(i)}(2,2)$ calculated using the original continued-fraction approach and obtained using the proposed method are given in Table IV. It is obvious, that

Table II. Numerically obtained eigenvalues λ_1–λ_{36} of scaled boundary finite element model of a sphere with 169 nodes (exact: $\lambda = l + 0.5$).

$\lambda_1-\lambda_{10}$ ($l=0,2,4,6$)	$\lambda_{11}-\lambda_{21}$ ($l=8,10$)	$\lambda_{22}-\lambda_{28}$ ($l=12$)	$\lambda_{29}-\lambda_{36}$ ($l=14$)
0.50000000000009	8.51533401465328	12.6118968242721	14.7421698347399
2.50004435105105	8.52032611434256	12.6186120918404	14.7685097861334
2.50010611746248	8.52936548138046	12.6582278013667	14.7852998602968
4.50097278992381	8.53657216440398	12.6684584865440	14.8659477980199
4.50134547749086	8.54440049469561	12.6977082935495	14.8977897906490
4.50183515569867	10.5444681431772	12.7784647321285	14.9260054079905
6.50411670019795	10.5502767359077	12.7934068783958	15.0931472966037
6.50713044737198	10.5679728628512		15.0952718474127
6.50978529092157	10.5843306859938		
6.51074937945877	10.6090377335465		
	10.6254795708898		

Table III. Scaled boundary finite element model of a sphere with 169 nodes: extremal singular values of $[c^{(i)}]$ calculated using the original continued-fraction approach [37].

i	1	2	3	4
$\sigma_{\min}$	1.688051973E−005	4.500840708E−002	3.677241646E−005	4.621796054E−002
$\sigma_{\max}$	16.1022314542765	62032887.2299980	14812.2894796318	1074627169.84942
$1/r_c$	1.048334188E−006	7.255571858E−010	2.482561289E−009	4.300836778E−011
i	5	6	7	8
$\sigma_{\min}$	2.118820415E−007	3.277440613E−002	2.755917872E−008	2.247243525E−002
$\sigma_{\max}$	19684.0896606832	26938940109.5397	27742.6869835749	161786153233.836
$1/r_c$	1.076412703E−011	1.216618249E−012	9.9338534628−013	1.389020927E−013
i	9	10	11	12
$\sigma_{\min}$	8.608016797E−008	4.003463675E−003	7.236656993E−004	0.54517352924665
$\sigma_{\max}$	16534.51841476760	50839023639.1364	4834254539.94627	1.151926263E+016
$1/r_c$	5.206088609E−012	7.874784739E−014	1.496954067E−013	4.732712039E−017

DOI: 10.1002/nme

Table IV. Scaled boundary finite element model of a sphere with 169 nodes: coefficients $[Y_0^{(i)}]$ calculated using original continued-fraction expansion of Reference [37] and proposed method.

i	Original approach [37] $\begin{bmatrix} Y_0^{(i)}(1,1) & Y_0^{(i)}(1,2) \\ Y_0^{(i)}(2,1) & Y_0^{(i)}(2,2) \end{bmatrix}$	Proposed method $\begin{bmatrix} Y_0^{(i)}(1,1) & Y_0^{(i)}(1,2) \\ Y_0^{(i)}(2,1) & Y_0^{(i)}(2,2) \end{bmatrix}$
1	$\begin{bmatrix} +0.1434154E+04 & +0.1437620E+04 \\ +0.1437620E+04 & +0.1435951E+04 \end{bmatrix}$	$\begin{bmatrix} -0.1999778E+01 & +0.6277101E-03 \\ +0.\ 6277101E-03 & -0\ .2000725E+01 \end{bmatrix}$
2	$\begin{bmatrix} +0.4600602E-02 & +0.6041999E-03 \\ +0.6041999E-03 & +0.8063793E-02 \end{bmatrix}$	$\begin{bmatrix} +0.4000113E+01 & -0.8120253E-03 \\ -0.8120253E-03 & +0.4001916E+01 \end{bmatrix}$
3	$\begin{bmatrix} +0.7104364E+04 & +0.7043817E+04 \\ +0.7043817E+04 & +0.6968549E+04 \end{bmatrix}$	$\begin{bmatrix} -0.5973630E+01 & +0.4963234E-01 \\ +0.4963234E-01 & -0\ .5947455E+01 \end{bmatrix}$
4	$\begin{bmatrix} -0.1699687E-01 & -0\ .5433733E-01 \\ -0.5433734E-01 & -0\ .1001392E+00 \end{bmatrix}$	$\begin{bmatrix} +0.7771816E+01 & -0.4400589E+00 \\ -0.4400589E+00 & +0.7510932E+01 \end{bmatrix}$
5	$\begin{bmatrix} +0.1006150E+04 & +0.2094670E+04 \\ +0.2094677E+04 & +0.3126565E+04 \end{bmatrix}$	$\begin{bmatrix} -0.9805336E+01 & +0.1332716E+00 \\ +0.1332716E+00 & -0.9911922E+01 \end{bmatrix}$
6	$\begin{bmatrix} -0.1293326E+00 & -0.2539840E+00 \\ -0.2539811E+00 & -0.4309366E+00 \end{bmatrix}$	$\begin{bmatrix} +0.1183400E+02 & -0.2054005E-01 \\ -0.2054005E-01 & +0.1190981E+02 \end{bmatrix}$
7	$\begin{bmatrix} +0.2154154E+07 & +0.2138973E+07 \\ +0.2133714E+07 & +0.2138346E+07 \end{bmatrix}$	$\begin{bmatrix} -0.1738691E+02 & -0\ .4909176E+00 \\ -0.4909176E+00 & -0\ .1391942E+02 \end{bmatrix}$
8	$\begin{bmatrix} -0.3704987E+00 & -0.3975387E+00 \\ -0.3995557E+00 & -0.4296733E+00 \end{bmatrix}$	$\begin{bmatrix} +0.2015699E+02 & +0.2630201E+01 \\ +0.2630201E+01 & +0.1842174E+02 \end{bmatrix}$
9	$\begin{bmatrix} -0.9120910E+07 & -0.9110289E+07 \\ -0.9193260E+07 & -0.9182902E+07 \end{bmatrix}$	$\begin{bmatrix} -0.1772112E+02 & +0.1395689E+01 \\ +0.1395689E+01 & -0.1785685E+02 \end{bmatrix}$

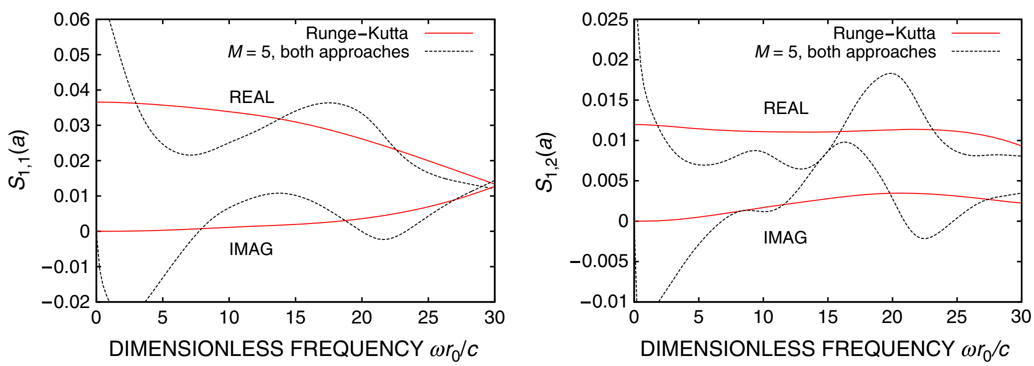

Figure 12. Continued-fraction solution of order $M = 5$ for impedance matrix of spherical cavity (diagonal term $S_{1,1}$ and off-diagonal term $S_{1,2}$).

the coefficients calculated using the original approach ([37]) are alternating in magnitude in each step of the recursive procedure. In this case, the calculation of the coefficients $[Y_0^{(i)}]$ and $[Y_1^{(i)}]$ is ill-conditioned. The corresponding error is such that the coefficients $[Y_0^{(i)}]$ and $[Y_1^{(i)}]$ are not symmetric for $i \geqslant 4$.

On the contrary, Table IV shows, that all coefficients calculated using the proposed method are roughly of the same order of magnitude, even for high degrees M. Symmetry is retained. It is also worth noting that the diagonal coefficients $Y_0^{(i)}$ are close to the coefficients obtained analytically for one mode of the spherical cavity in Section 3.2, Equation (73), that is $Y_0^{(i)} = \pm 2, \pm 4, \pm 6, \ldots$, for the first few steps of the recursive procedure.

The accuracy in the frequency domain of the two continued-fraction solutions of Equation (10) is evaluated in Figures 12–14. As an example, the diagonal term $S_{1,1}$ and the off-diagonal term

DOI: 10.1002/nme

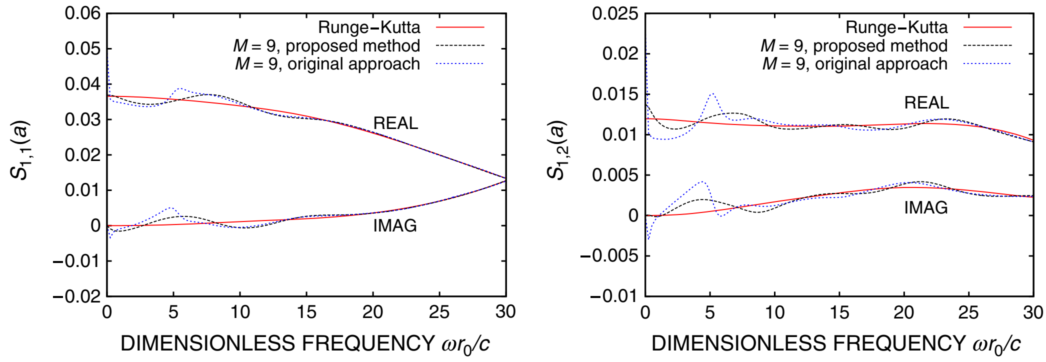

Figure 13. Continued-fraction solution of order $M = 9$ for impedance matrix of spherical cavity (diagonal term $S_{1,1}$ and off-diagonal term $S_{1,2}$).

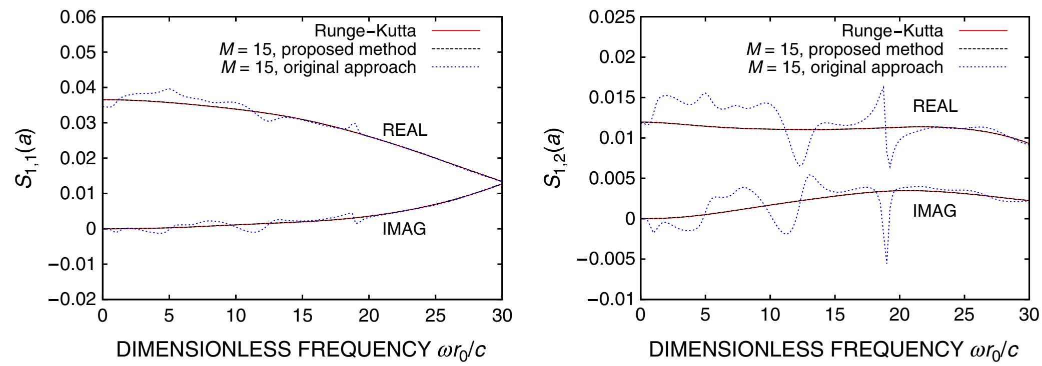

Figure 14. Continued-fraction solution of order $M = 15$ for impedance matrix of spherical cavity (diagonal term $S_{1,1}$ and off-diagonal term $S_{1,2}$).

$S_{1,2}$ of the 169×169 impedance matrix $[S^{\infty}]$ are shown. The continued-fraction solutions of order $M = 5$, $M = 9$ and $M = 15$ are compared with the impedance calculated by numerical integration of Equation (10) in Figures 12, 13 and 14, respectively.

For low degrees of continued-fraction expansion, the two continued-fraction solutions obtained using the original approach [37] or the proposed method are identical, as is shown in Figure 12 for $M = 5$. The continued-fraction solution of order $M = 5$, however, differs strongly from the reference solution in the low-frequency range, because of the low order of expansion. Figure 13 shows that increasing the order of expansion to $M = 9$ leads to a significant improvement, if the proposed method is used. The resulting impedance curve is smooth and approaches the exact curve. On the contrary, the continued-fraction solution calculated using the original approach [37] is clearly more irregular and differs strongly from the reference solution for low frequencies. As explained earlier, the original approach of Reference [37] leads to ill-conditioning for high degrees of approximation and large numbers of DOF. Higher-order terms $[Y_0^{(i)}]$ and $[Y_1^{(i)}]$ are calculated with lower accuracy, the continued-fraction expansion diverges. This is obviously not the case for the proposed alternative continued-fraction solution. Figure 14 confirms this observation. The original continued-fraction solution of degree $M = 15$ of Reference [37] differs considerably from the exact curve in the low-frequency range; no convergence is achieved. On the contrary, the agreement between the exact curve and the continued-fraction solution calculated using the proposed method is excellent.

The superiority of the proposed method with respect to accuracy is further illustrated in Figure 15. An error measure is shown, which is defined as follows. The difference $[S_{\Delta}]$ of the impedance matrix constructed using the continued-fraction solution from the impedance matrix obtained by numerical

DOI: 10.1002/nme

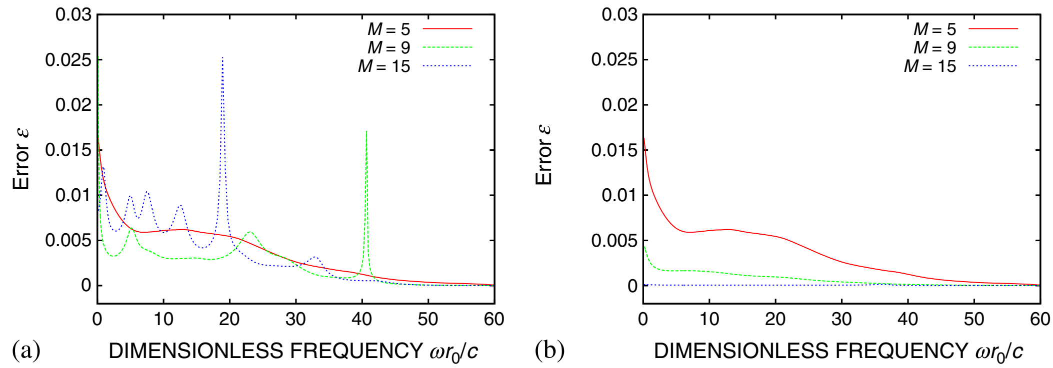

Figure 15. Error ε in impedance of spherical cavity. (a) Original approach [37] and (b) Proposed method.

integration of Equation (10) is calculated.

$$[S_\Delta] = [S^\infty_{RK}] - [S^\infty_{CF}], \qquad \begin{array}{l}\text{index RK} - \text{Runge–Kutta}\\ \text{index CF} - \text{Continued Fraction}\end{array} \tag{100}$$

The error ε is defined as the scalar norm of the matrix $[S_\Delta]$ divided by the number of DOFs n,

$$\varepsilon = \frac{\|[S_\Delta]\|}{n}. \tag{101}$$

The square of the scalar norm of a complex matrix of order n is defined as the sum of the scalar products of its rows $[s^l_{\Delta,re}]$ and $[s^l_{\Delta,im}]$:

$$[S_\Delta] = [S_{\Delta,re}] + \mathrm{i}[S_{\Delta,im}], \quad [S_{\Delta,re}] = \begin{bmatrix} [s^1_{\Delta,re}] \\ [s^2_{\Delta,re}] \\ \vdots \\ [s^n_{\Delta,re}] \end{bmatrix}, \quad [S_{\Delta,im}] = \begin{bmatrix} [s^1_{\Delta,im}] \\ [s^2_{\Delta,im}] \\ \vdots \\ [s^n_{\Delta,im}] \end{bmatrix}. \tag{102}$$

$$\|[S_\Delta]\|^2 = \sum_{l=1}^{n} [s^l_{\Delta,re}][s^l_{\Delta,re}]^T + [s^l_{\Delta,im}][s^l_{\Delta,im}]^T. \tag{103}$$

Figure 15(a) and (b) corresponds to the results obtained using the original approach [37] and the proposed method, respectively. In general, the error approaches zero for high frequencies, because of the high-asymptotic nature of the continued-fraction solution. As observed in Figure 12, both approaches yield an identical error curve for $M = 5$. However, clear differences can be seen for higher orders of expansion M. Figure 15 shows that for $M = 9$ and $M = 15$, the error obtained using the original approach is considerably higher than ε corresponding to the proposed method. The error curves corresponding to the original approach [37] do not converge for increasing M. On the contrary, ε approaches zero for high orders of expansion M if the proposed method is used, as is clearly shown in Figure 15(b).

5.3. Three-dimensional elastic foundation embedded in homogeneous isotropic halfspace

As a 3D vector-valued problem, vertical motion of a square foundation $2b \times 2b$ embedded with depth $e = 2/3b$ in a homogeneous isotropic halfspace is analysed. The system is shown in Figure 16. Assuming symmetry, only one quarter is modelled using the SBFEM. The foundation-soil interface is meshed with 12 8-node SBFEs, leading to a total of 129 DOFs.

The continued-fraction solution for the dynamic stiffness matrix $[S^\infty]$ is constructed using the proposed method or the original approach presented in Reference [37]. The accuracy in the frequency domain is evaluated in Figures 17–19. As an example, the diagonal term $S_{1,1}$ and the

DOI: 10.1002/nme

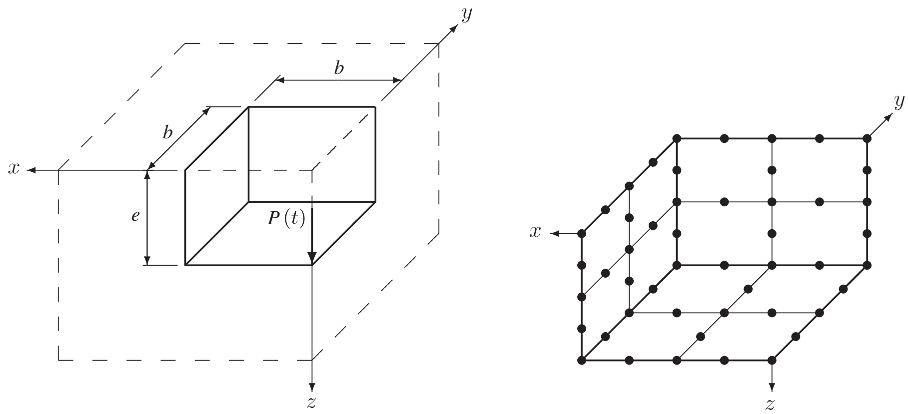

Figure 16. One quarter of a square foundation embedded in homogeneous halfspace; geometry and mesh.

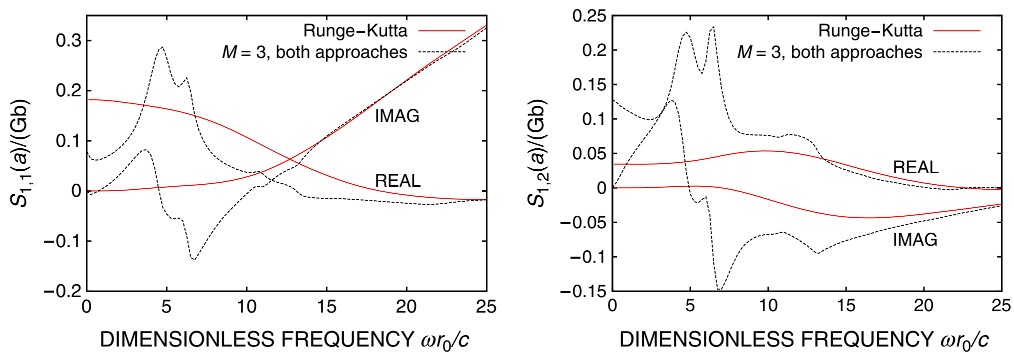

Figure 17. Continued-fraction solution of order $M = 3$ for dynamic stiffness matrix of embedded square foundation (diagonal term $S_{1,1}$ and off-diagonal term $S_{1,2}$).

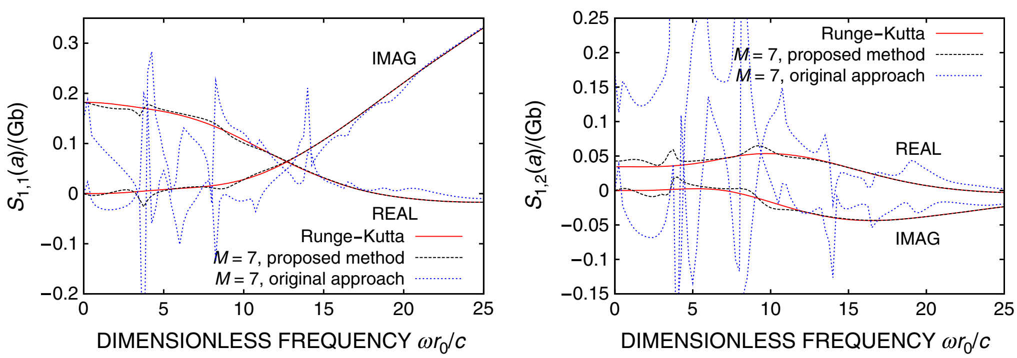

Figure 18. Continued-fraction solution of order $M = 7$ for dynamic stiffness matrix of embedded square foundation (diagonal term $S_{1,1}$ and off-diagonal term $S_{1,2}$).

off-diagonal term $S_{1,2}$ of the 129×129 dynamic stiffness matrix $[S^{\infty}]$ are shown in a dimensionless form. The continued-fraction solutions of order $M = 3$, $M = 7$ and $M = 10$ and 17 are compared with the dynamic stiffness obtained by numerical integration of Equation (10) in Figures 17, 18 and 19, respectively.

Similar conclusions as in the previous example can be drawn. For $M = 3$, the two continued-fraction solutions obtained using the original approach [37] or the proposed method are identical, as is shown in Figure 17. This low-order continued-fraction solution, however, differs strongly from the reference solution in the low-frequency range. The agreement between the dynamic stiffness

DOI: 10.1002/nme

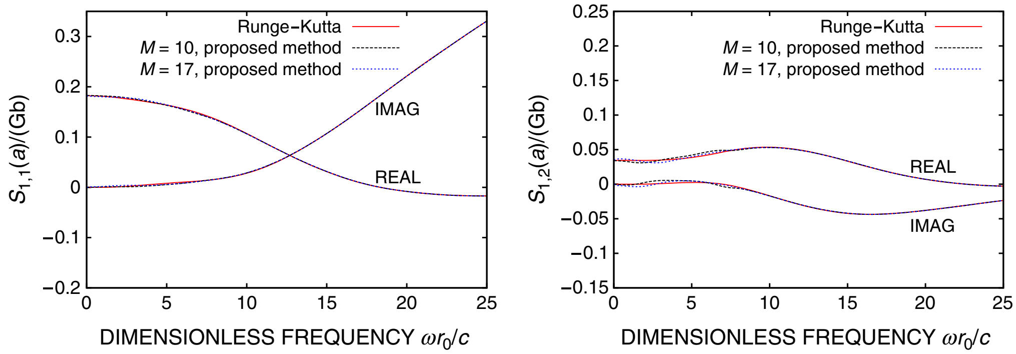

Figure 19. Continued-fraction solution of order $M = 10$ and $M = 17$ for dynamic stiffness matrix of embedded square foundation (diagonal term $S_{1,1}$ and off-diagonal term $S_{1,2}$).

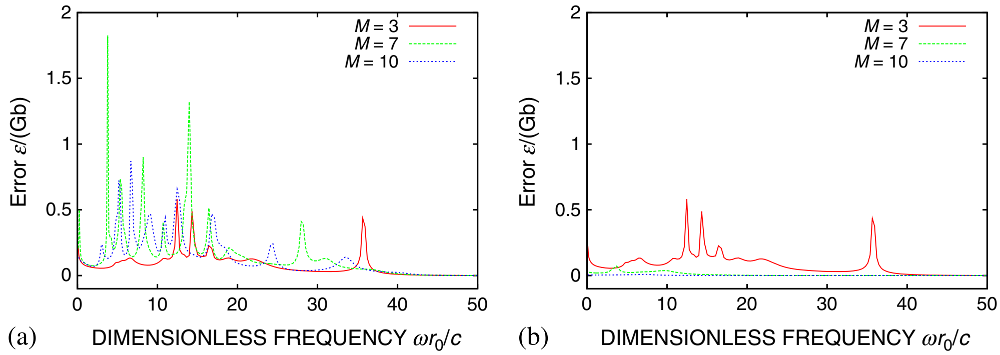

Figure 20. Error ε in dynamic stiffness of embedded square foundation.(a) Original approach [37] and (b) Proposed method.

obtained by numerical integration and the continued-fraction solution is improved significantly, if the proposed method is used to calculate the coefficients $[Y_0^{(i)}]$ and $[Y_1^{(i)}]$ of an order $M = 7$ approximation, as can be seen in Figure 18. On the contrary, the continued-fraction solution of order $M = 7$ calculated using the original approach [37] is clearly erroneous. Since the continued-fraction solution of [37] diverges for $M \geqslant 5$, it is not shown for higher orders of M. Figure 19 confirms that the proposed continued-fraction expansion converges to the exact solution for increasing order M.

The error in dynamic stiffness as defined in Equations (100), (101) and (103) is evaluated and shown in Figure 20. Analogous conclusions as in Section 5.2 can be drawn. For a very low degree of expansion $M = 3$, the error curves corresponding to the two different approaches are identical. The error diverges for increasing M if the original approach [37] is used, whereas ε approaches zero for higher orders of expansion M in the proposed method.

The transient response of the 3D soil halfspace with excavation (no foundation), initially at rest, is evaluated. In the time domain, the unbounded domain is described by the system of first-order differential equations (96). It is assumed that a vertical force $P(t)$ acts at the bottom centre of the foundation ($x = 0$, $y = 0$, $z = e$). The time-dependence of the excitation is prescribed as a Ricker wavelet. The time history of the Ricker wavelet is given as

$$P(t) = P_0 \left(1 - 2\left(\frac{t - t_s}{t_0}\right)^2\right) \exp\left(-\left(\frac{t - t_s}{t_0}\right)^2\right), \tag{104}$$

where t_s is the time when the wavelet reaches its maximum, $2/t_0$ is the dominant angular frequency of the wavelet and P_0 is the amplitude. A Ricker wavelet with the parameters $\bar{t}_s = t_s \frac{c_s}{b} = 1$, $\bar{t}_0 = t_0 \frac{c_s}{b} = 0.2$ and $P_0 = 10^5$ N is considered. The resulting transient displacements of the foundation-soil interface are calculated solving Equation (96) using a standard time-stepping scheme. The time-step size is chosen as $\Delta t = t_s/200$. The matrices $[A]$ and $[B]$ of Equation (96)

DOI: 10.1002/nme

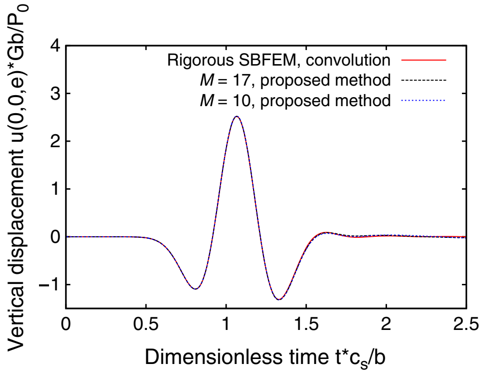

Figure 21. Displacement response of halfspace with square excavation to a vertical force applied as a Ricker wavelet (Equation (104)) at ($x = 0$, $y = 0$, $z = e$).

result from a numerical process, involving repeated inversion. Unfortunately, it cannot be guaranteed a priori that all homogeneous solutions of the system (96) are decaying. However, possible spurious modes can be identified by means of an algebraic eigenvalue problem and removed from the solution space in an a posteriori manner by means of a spectral shifting procedure. For details, the reader is referred to Reference [41].

Figure 21 shows the computed vertical displacement at the bottom centre of the foundation. The results are non-dimensionalised with P_0/Gb. The displacement response obtained using the proposed continued-fraction solution of order $M = 10$ and of order $M = 17$ is compared with the numerical result calculated using the rigorous SBFEM based on convolution. In the rigorous analysis, the time-step $\Delta t = 0.005b/c_s$ is selected. The agreement between the result of the rigorous analysis based on convolution and that of the present transmitting boundary is excellent for $t < 1.5b/c_s$. After that, very small differences occur. These deviations are due to the fact that the proposed singly-asymptotic transmitting boundary approximates the high-frequency behaviour with higher accuracy than the static stiffness. The accuracy in the time domain can be further improved by further increasing the order of continued-fraction expansion M.

6. CONCLUSIONS

A high-order local transmitting boundary for the modelling of wave propagation in unbounded domains of arbitrary geometry is developed. It is based on a continued-fraction expansion of the dynamic stiffness matrix of an unbounded domain. An improved continued-fraction solution is proposed, which is computationally more robust than a previous procedure [37]. It is characterised by an additional, matrix-valued factor. Based on the analysis of a model problem with an analytical solution, this additional factor is chosen such that singularities are removed. Numerical examples demonstrate that the improved continued-fraction expansion converges to the exact dynamic stiffness for increasing orders of expansion M. The proposed procedure is successfully applied to systems with a large number of DOFs. No ill-conditioning is observed, even for very high orders of approximation M. Thus, the proposed improved continued-fraction expansion is suitable for large-scale systems.

The coefficient matrices of the continued-fraction solution are calculated recursively, directly from the SBFE equation in dynamic stiffness. The computationally expensive numerical integration of these equations is thus avoided. The continued-fraction solution in the frequency domain corresponds to a system of first-order differential equations in the time domain with symmetric banded frequency-independent matrices. It can be coupled with the equations of motion of the near field straightforwardly. Coupled systems including unbounded domains of arbitrary geometry can thus be analysed directly in the time domain using standard procedures.

Although the proposed method is suitable for systems with many DOFs, it should be noted that the order of expansion M required to achieve a given accuracy is proportional to the mode number

DOI: 10.1002/nme

and thus the number of unknowns. This can be improved by using a doubly-asymptotic expansion. Such a formulation has been successfully developed for scalar waves in Reference [52]. Research on its extension to vector waves in unbounded domains of arbitrary geometry and in layered systems is in progress.

ACKNOWLEDGEMENTS

Part of the research reported herein was supported by a Marie Curie International Outgoing Fellowship of the first author within the 7th European Community Framework Programme. The financial support provided by the European Union is gratefully acknowledged.

REFERENCES

1. Kausel E. Local transmitting boundaries. *Journal of Engineering Mechanics* 1988; **114**(6):1011–1027.
2. Givoli D. Non-reflecting boundary conditions. *Journal of Computational Physics* 1991; **94**:1–29.
3. Givoli D. Exact representations on artificial interfaces and applications in mechanics. *Applied Mechanics Reviews* 1999; **52**(11):333–349.
4. Tsynkov SV. Numerical solution of problems on unbounded domains. A review. *Applied Numerical Mathematics* 1998; **27**:465–532.
5. Astley RJ. Infinite elements for wave problems: a review of current formulations and an assessment of accuracy. *International Journal for Numerical Methods in Engineering* 2000; **49**:951–976.
6. Givoli D. High-order local non-reflecting boundary conditions: a review. *Wave Motion* 2004; **39**:319–326.
7. Beskos DE. Boundary element methods in dynamic analysis. *Applied Mechanics Reviews* 1987; **40**:1–23.
8. Beskos DE. Boundary element methods in dynamic analysis: Part II (1986 –1996). *Applied Mechanics Reviews* 1997; **50**:149–197.
9. Kausel E, Roesset JM. Dynamic stiffness of circular foundations. *Journal of the Engineering Mechanics Division* 1975; **101**:771–785.
10. Kausel E, Peek R. Dynamic loads in the interior of a layered stratum: an explicit solution. *Bulletin of the Seismological Society of America* 1982; **72**:1459–1481.
11. Kausel E. Wave propagation in anisotropic layered media. *International Journal for Numerical Methods in Engineering* 1986; **23**:1567–1578.
12. Seale SH, Kausel E. Point loads in cross-anisotropic layered halfspaces. *Journal of Engineering Mechanics* 1989; **115**:509–542.
13. Kausel E. Thin-layer method: formulation in the time domain. *International Journal for Numerical Methods in Engineering* 1994; **37**:927–941.
14. Keller JB, Givoli D. Exact non-reflecting boundary conditions. *Journal of Computational Physics* 1989; **82**:172–192.
15. Lysmer J, Kuhlemeyer RL. Finite dynamic model for infinite media. *Journal of the Engineering Mechanics Division* 1969; **95**(4):859–878.
16. Bettess P. *Infinite Elements*. Penshaw Press: Sunderland, 1992.
17. Berenger JP. A perfectly matched layer for the absorption of electromagnetic waves. *Journal of Computational Physics* 1994; **114**:185–200.
18. Engquist B, Majda A. Absorbing boundary conditions for the numerical simulation of waves. *Mathematics of Computation* 1977; **31**(139):629–651.
19. Engquist B, Majda A. Radiation boundary conditions for acoustic and elastic wave calculations. *Communications on Pure and Applied Mathematics* 1979; **32**:313–357.
20. Bayliss A, Gunzburger M, Turkel E. Boundary conditions for the numerical solution of elliptic equations in exterior regions. *SIAM Journal of Applied Mathematics* 1982; **42**:430–451.
21. Higdon RL. Absorbing boundary conditions for difference approximations to the multi-dimensional wave equation. *Mathematics of Computation* 1986; **47**(176):437–459.
22. Wolf JP. *Soil-structure-interaction analysis in time domain*. Prentice-Hall, Inc.: Englewood Cliffs, NJ, 1988.
23. Grote MJ, Keller JB. Exact nonreflecting boundary conditions for the time dependent wave equation. *SIAM Journal of Applied Mathematics* 1995; **55**:280–297.
24. Grote MJ, Keller JB. Exact nonreflecting boundary condition for elastic waves. *SIAM Journal of Applied Mathematics* 2000; **60**:803–819.
25. Grote MJ. Local nonreflecting boundary condition for Maxwell's equations. *Computer Methods in Applied Mechanics and Engineering* 2006; **195**:3691–3708.
26. Hagstrom T, Hariharan SI. A formulation of asymptotic and exact boundary conditions using local operators. *Applied Numerical Mathematics* 1998; **27**:403–416.
27. Huan R, Thompson LL. Accurate radiation boundary conditions for the time-dependent wave equation on unbounded domains. *International Journal for Numerical Methods in Engineering* 2000; **47**:1569–1603.
28. Thompson LL, Huan R, He D. Accurate radiation boundary conditions for the two-dimensional wave equation on unbounded domains. *Computer Methods in Applied Mechanics and Engineering* 2001; **191**:311–351.

29. Krenk S. Unified formulation of radiation conditions for the wave equation. *International Journal for Numerical Methods in Engineering* 2002; **53**:275–295.
30. Guddati MN, Tassoulas JL. Continued-fraction absorbing boundary conditions for the wave equation. *Journal of Computational Acoustics* 2000; **8**(1):139–156.
31. Guddati MN, Lim KW. Continued fraction absorbing boundary conditions for convex polygonal domains. *International Journal for Numerical Methods in Engineering* 2006; **66**:949–977.
32. Givoli D, Patlashenko I. An optimal high-order non-reflecting finite element scheme for wave scattering problems. *International Journal for Numerical Methods in Engineering* 2002; **53**:2389–2411.
33. Givoli D, Neta B. High-order non-reflecting boundary scheme for time-dependent waves. *Journal of Computational Physics* 2003; **186**:24–46.
34. Hagstrom T, Warburton T. A new auxiliary variable formulation of high-order local radiation boundary conditions: corner compatibility conditions and extensions to first-order systems. *Wave Motion* 2004; **39**:327–338.
35. van Joolen VJ, Neta B, Givoli D. High-order Higdon-like boundary conditions for exterior transient wave problems. *International Journal for Numerical Methods in Engineering* 2005; **63**:1041–1068.
36. Kechroud R, Antoine X, Soulaimani A. Numerical accuracy of a Padé-type non-reflecting boundary condition for the finite element solution of acoustic scattering problems at high-frequency. *International Journal for Numerical Methods in Engineering* 2005; **64**:1275–1302.
37. Bazyar MH, Song C. A continued-fraction-based high-order transmitting boundary for wave propagation in unbounded domains of arbitrary geometry. *International Journal for Numerical Methods in Engineering* 2008; **74**:209–237.
38. Wolf JP. Consistent lumped-parameter models for unbounded soil: Physical representation. *Earthquake Engineering and Structural Dynamics* 1991; **20**:11–32.
39. Wolf JP. Consistent lumped-parameter models for unbounded soil: frequency-independent stiffness, damping and mass matrices. *Earthquake Engineering and Structural Dynamics* 1991; **20**:33–41.
40. Ruge P, Trinks C, Witte S. Time-domain analysis of unbounded media using mixed-variable formulations. *Earthquake Engineering and Structural Dynamics* 2001; **30**:899–925.
41. Trinks C. Consistent absorbing boundaries for time-domain interaction analyses using the fractional calculus. *Ph.D. Thesis*, Technische Universität Dresden, Fakultät Bauingenieurwesen, 2004.
42. Wolf JP. *The Scaled Boundary Finite Element Method*. Wiley & Sons: Chichester, 2003.
43. Song C, Wolf JP. The scaled boundary finite-element method–alias consistent infinitesimal finite-element cell method–for elastodynamics. *Computer Methods in Applied Mechanics and Engineering* 1997; **147**:329–355.
44. Bazyar MH, Song C. Time-harmonic response of non-homogeneous elastic unbounded domains using the scaled boundary finite-element method. *Earthquake Engineering and Structural Dynamics* 2006; **35**:357–383.
45. Bazyar MH, Song C. Transient analysis of wave propagation in non-homogeneous elastic unbounded domains by using the scaled boundary finite-element method. *Earthquake Engineering and Structural Dynamics* 2006; **35**:1787–1806.
46. Song C, Bazyar MH. A boundary condition in Padé series for frequency-domain solution of wave propagation in unbounded domains. *International Journal for Numerical Methods in Engineering* 2007; **69**:2330–2358.
47. Song C, Bazyar MH. Development of a fundamental-solution-less boundary element method for exterior wave problems. *Communications in Numerical Methods in Engineering* 2008; **24**:257–279.
48. Birk C. Time-domain analysis of wave propagation in unbounded domains based on the scaled boundary finite element method. *Proceedings of Applied Mathematics and Mechanics* 2009; **9**:91–94.
49. Wolf JP, Song C. The scaled boundary finite-element method–a primer: derivations. *Computers and Structures* 2000; **78**:191–210.
50. Wolf JP, Song C. *Finite-Element Modelling of Unbounded Media*. John Wiley & Sons: Chichester, 1996.
51. Jonsson T, Yngvason J. *Waves and Distributions*. World Scientific: Singapore, 1995.
52. Prempramote S, Song C, Tin-Loi F, Lin G. High-order doubly asymptotic open boundaries for scalar wave equation. *International Journal for Numerical Methods in Engineering* 2009; **79**:340–374.
53. Golub GH, Van Loan CF. *Matrix Computations*. North Oxford Academic: Oxford, 1983.
54. Song C. A matrix function solution for the scaled boundary finite-element equation in statics. *Computer Methods in Applied Mechanics and Engineering* 2004; **193**:2325–2356.
55. Press WH, Flannery BP, Teukolsky SA. *Numerical Recipes in FORTRAN 77: The Art of Scientific Computing*, Vol. 1. Cambridge University Press: Cambridge, 1992.

DOI: 10.1002/nme